LA-UR-11-10385
Approved for public release; distribution is unlimited.

Title: Simulation of CO2 Sequestration at Rock Spring Uplift, Wyoming: Heterogeneity and Uncertainties in Storage Capacity, Injectivity and Leakage

Author(s): Deng, Hailin
Dai, Zhenxue
Jiao, Zunsheng
Stauffer, Philip H.
Surdam, Ronald C.

Intended for: International Journal of Greenhouse Gas Control
10th Annual CCS conference, 2011-05-02/2011-05-05 (Pittsburgh, Pennsylvania, United States)

# Simulation of $CO_2$ Sequestration at Rock Spring Uplift, Wyoming: Heterogeneity and Uncertainties in Storage Capacity, Injectivity and Leakage

Hailin Deng[a], Philip H. Stauffer[a*], Zhenxue Dai[a], Zunsheng Jiao[b], Ronald C. Surdam[b]

[a] Los Alamos National Laboratory, EES-16, Mail Stop T-003 Los Alamos, NM 87544, USA

[b] Wyoming State Geological Survey, University Campus Laramie, WY 82071, USA

* Corresponding author: stauffer@lanl.gov; Tel: 1-505-665-4638; Fax: 1-505-665-8737

**Keywords:** $CO_2$ sequestration; Storage Capacity; Heterogeneity; Transition Probability; Uncertainty; Rock Spring Uplift

Submitted to ***International Journal of Greenhouse Gas Control***

April 2011

## Abstract

Many geological, geochemical, geomechanical and hydrogeological factors control $CO_2$ storage in subsurface. Among them heterogeneity in saline aquifer can seriously influence design of injection wells, $CO_2$ injection rate, $CO_2$ plume migration, storage capacity, and potential leakage and risk assessment. This study applies indicator geostatistics, transition probability and Markov chain model at the Rock Springs Uplift, Wyoming generating facies-based heterogeneous fields for porosity and permeability in target saline aquifer (Pennsylvanian Weber sandstone) and surrounding rocks (Phosphoria, Madison and cap-rock Chugwater). A multiphase flow simulator FEHM is then used to model injection of $CO_2$ into the target saline aquifer involving field-scale heterogeneity. The results reveal that (1) $CO_2$ injection rates in different injection wells significantly change with local permeability distributions; (2) brine production rates in different pumping wells are also significantly impacted by the spatial heterogeneity in permeability; (3) liquid pressure evolution during and after $CO_2$ injection in saline aquifer varies greatly for different realizations of random permeability fields, and this has potential important effects on hydraulic fracturing of the reservoir rock, reactivation of pre-existing faults and the integrity of the cap-rock; (4) $CO_2$ storage capacity estimate for Rock Springs Uplift is 6614 ± 256 Mt at 95% confidence interval, which is about 36% of previous estimate based on homogeneous and isotropic storage formation; (5) density profiles show that the density of injected $CO_2$ below 3 km is close to that of the ambient brine with given geothermal gradient and brine concentration, which indicates $CO_2$ plume can sink to the deep before reaching thermal equilibrium with brine. Finally, we present uncertainty analysis of $CO_2$ leakage into overlying formations due to heterogeneity in both the target saline aquifer and surrounding formations. This uncertainty in leakage will be used to feed into risk assessment modeling.

## 1. Introduction

Geological $CO_2$ sequestration (GCS) in subsurface saline water reservoir is a practical way among several approaches to reduce release of anthropogenic $CO_2$ into the atmosphere and mitigate global warming (Friedmann, 2003; Benson & Cole, 2008; Bickle, 2009; & Nordbotten, 2009). In order to take an action making GCS become a real business in the world, many pilot sites have been demonstrated, studied and operated through projects funded by US Department of Energy (DOE) and other country's governments (Michael et al., 2010). Among them Rock Springs Uplift (RSU) in the southwestern Wyoming, USA has been identified as an ideal site for GCS by Wyoming State Geological Survey (Surdam et al., 2007; Surdam et al., 2009). Initial estimation of storage capacity for GCS based on hypothetical homogeneous storage formation shows RSU can totally sequester 26 billion tons of $CO_2$, with storage of 54 million tons per year for 485 years (Surdam et al., 2007). With progresses made at RSU (Stauffer et al., 2010; Deng et al., 2010a), new numerical simulations involving spatial heterogeneity in storage formation and cap-rock are performed with special respect to reevaluation of storage capacity, well injectivity and well design in order to shed light on GCS at RSU.

GCS is a very complex system (Friedmann, 2007; Celia & Nordbotten, 2009). Many geological (Ambrose et al., 2008; Michael et al., 2010), hydrological (Bachu et al., 1994; Tsang et al., 2008; Person et al., 2010), geochemical (Xu et al., 2004; Kharaka et al., 2006; Gaus, 2010; Wilkin & Digiulio, 2010), and geomechanical (Lucier et al., 2006; Rutqvist et al., 2008; Deng et al., 2010b) factors control $CO_2$ storage. Among them heterogeneity in the saline water reservoir can seriously influence design of injection wells (Deng et al., 2010a), $CO_2$ injection rate (Stauffer et al., 2009a), $CO_2$ plume migration (Flett et al., 2007), storage capacity (CSFL Task Force, 2008), and potential leakage and risk assessment (Stauffer et al., 2009b; Flett et al., 2007;

Liu & Zhang, 2011). Therefore, any site-specified simulations of geological sequestration of $CO_2$ need to incorporate heterogeneity structure into their models (Doughty & Pruess, 2004; Schnaar & Digiulio, 2009) in order to gain insights into site-specified storage.

Storage capacity is one of the central issues in GCS (Bachu et al., 2007) because not only governments need reliable estimation to make decision about policies and regulations, but also industry needs robust estimation for business decision (Bradshaw et al., 2007). The methodologies to estimate and evaluate the storage capacity in saline aquifers have been developed or summarized by different researchers and teams (USDOE, 2007; Bachu et al., 2007; CSLF task force, 2008; Ambrose et al., 2008; Zhou et al., 2008; Miller et al., 2010; Juanes et al., 2010). However, they are highly variable due to many levels of uncertainty associated with assumptions for different trapping mechanisms (structural-stratigraphic, residual-gas, solubility, mineral and hydrodynamic traps). Zhou et al. (2008) developed an analytical method for quick assessment of storage capacity in closed and semi-closed saline aquifers, which complements the methods for capacity estimation in open saline aquifers. As for GCS in a closed underground volume, Ehlig-Economides & Economides (2010) argued that the volume of liquid or supercritical $CO_2$ to be stored could not be larger than about 1% of pore space and the increasing reservoir pressure would cause injection rate to undergo exponential decline. Therefore, GCS would be not feasible at any cost. Cavanagh et al. (2010) questioned the arguments of Ehlig-Economides & Economides (2010) that GCS is assumed in a closed system without pressure management. As shown by numerous evidences, GCS mainly targets the open saline aquifers, and pressure management can be done by brine production (Surdam et al., 2009). USDOE (2007) proposed a method involving a “storage efficient factor”, which is not easy to justify (Equation (1)):

$$M_{CO_2} = A \times h \times \phi \times \rho \times E \quad (1)$$

Where $M_{CO2}$ is the estimated $CO_2$ mass for storage capacity, $A$, $h$ and $\phi$ are area, average thickness and porosity of the saline aquifer, respectively; $\rho$ is the average $CO_2$ density under representative storage conditions of temperature and pressure, and $E$ is the storage efficient coefficient accounting for total pore volume filled with $CO_2$. Juanes et al. (2010) derived an analytical expression of storage efficiency for capillary trapping $CO_2$ in a homogeneous isotropic saline aquifer in a basin scale. Bachu et al. (2007) suggested a systematic approach to calculate storage capacity in deep saline aquifers, in which the equation for structural and stratigraphic trapping $CO_2$ (Equation (2)) is basically equivalent to the Equation (1):

$$M_{CO_2} = A \times h \times \phi \times \rho(P,T) \times (1 - S_{wi}) \times C_c \quad (2)$$

Where $S_{wi}$ is irreducible water saturation and $C_c$ is the capacity coefficient that integrates effects of trap heterogeneity, $CO_2$ buoyancy and sweep efficiency. They clearly distinguished different trapping mechanisms that corresponded to different estimation methods. For solubility traps, the storage capacity is estimated as:

$$M_{CO_2} = \iiint \phi \times \left(\rho_s X_S^{CO_2} - \rho_0 X_0^{CO_2}\right) dxdydz \quad (3)$$

Where $\rho$ and $X_{CO2}$ are density and the mass fraction of $CO_2$ in brine, respectively; the subscript $S$ and 0 denote $CO_2$ content at saturation and initial $CO_2$ content, which depends on temperature, pressure and salinity in storage formation. Because such parameters as depth, temperature, pressure, salinity, the storage efficient factor ($E$), the capacity coefficient ($C_c$), density of $CO_2$ fluid ($\rho$), brine density ($\rho_S$, $\rho_0$) and the mass fraction of $CO_2$ in brine ($X_0^{CO2}$, $X_S^{CO2}$) change with location by location when storage formations are irregular and heterogeneous, it is impossible to make a reliable estimation of the storage capacity through the simple analytical solutions (for example equation (1) and (2)). Three dimensional (3D) numerical solutions must be applied to

obtain reliable estimation of the storage capacity. However, a full-size 3D reservoir simulation is time consuming and computation intensive.

Assessment of $CO_2$ leakage from storage formation through boreholes (Viswanathan et al., 2008; Corey et al., 2010; Celia et al., 2011), fractures and faults (Rutqvist et al., 2008; Lucier et al., 2010; Lucier et al., 2008) to surface or into fresh water aquifers (Newmark et al., 2010) is necessary for CGS not only to win understanding and support from the public, but also to provide administrators with right information to establish reliable justification and regulation. Uncertainty analysis of $CO_2$ leakage can supply important information for how, where and when to monitor $CO_2$. So far many studies related to uncertainty analysis and risk assessment of $CO_2$ leakage focus on simple and homogeneous storage formation-cap-rock systems. Of course, through simplified and homogeneous system, preliminary assessment results are acquired cheaply and quickly. It is a necessary preliminary step to gain basic understanding of uncertainties and risks associated with CGS. However, if ones need to evaluate site-specified uncertainties and risks with CGS, 3D spatial heterogeneity must be incorporated into models. Such assessment results would be different from the homogeneous scenarios based on levels of complexity because where pore pressure builds up too high and where $CO_2$ plume migrates are constrained by 3D heterogeneity structures of porosity and permeability in reservoirs.

In this study, a field-scale heterogeneous reservoir model is first used at RSU to fully evaluate CGS, where production wells are designed to reduce fluid pressure and increase storage capacity; a practical numerical method is proposed to evaluate storage capacity, assess well injectivity, and analyze uncertainty in leakage under a scenario involving spatial heterogeneity of porosity and permeability in storage formation and cap-rock at RSU; density profile of supercritical $CO_2$ is also examined with relation to growth and migration of $CO_2$ plume. Geomechanical effects are

ignored here. Neither faulting cap-rocks nor reactivation of preexisting faults is considered. In this paper, after the introduction to geological setting of RSU, we present our methodology to characterize heterogeneity and procedure to conduct numerical simulation using a finite element heat and mass transport simulator (FEHM), then show results followed by discussion and conclusion.

## 2. Geological Setting of Rock Springs Uplift, Wyoming

Located in the southwestern Wyoming (Fig.1), the Rock Springs Uplift (RSU), an asymmetric doubly-plunging anticline with over 3000 m of closed structure relief (Surdam et al., 2007), lies on the Rocky Mountain foreland basement. This north-south trending large complex uplift separates the Greater Green River Basin into two equal parts: to the west are the Green River Basin and the Bridger Basin, and to the east are the Washakie Basin and the Great Divide Basin. The size of RSU is 50 miles long from south to north and 35 miles wide from west to east. The western flank of RSU dips more steeply than its eastern flank (Fig.2). There are many east- and northeast-trending faults cutting RSU on surface while a westward-oriented thrust fault on the western flank occurs at depth below the surface. The latter is thought as a sealed fault. Although the oldest rock in RSU is the Precambrian metamorphic bedrock in the core, above which there are Paleozoic, Mesozoic and Cenozoic formations (Fig.2 & 3), the oldest rocks exposed in the center of RSU are Cretaceous marine shales and sandstones because the Laramide tectonic event that formed RSU during Late Cretaceous and early Tertiary did not raise RSU high enough to expose the Precambrian core.

The Early Jurassic Nugget sandstone is massive to coarsely cross bedded, well-sorted, very-fine- to coarse-grained, quartz-rich sandstone with thickness of 30 to 150 m. The Cretaceous

Chugwater formation, a thick low-permeability stratigraphic unit (300 - 400 m thick), consists of interbedded red siltstone, shale, and fine-grained sandstone (Clarey et al., 2010; Surdam et al., 2009). The Permian Phosphoria formation just above the Pennsylvanian Weber sandstone varies in lithology from shaly siltstone to limestone interbedded with dolomite-siltstone due to sedimentary facies transition from organic, chert and phosphorite rich black shale to the west of RSU to carbonate to the east of RSU (Hein et al., 2004; Piper & Link, 2002). Therefore, Phosphoria can be a source rock, a storage reservoir or cap-rock depending on its local lithology. The Pennsylvanian Weber Sandstone is composed of a fine to medium-grained sandstone primarily deposited as cross-bedded sand dunes. The Mississippian Madison Limestone consists of massive limestone and dolomite with gray cherty limestone and dolomite, a shallow to moderately deep marine deposit up to 150 m thick. The Nugget sandstone, the Weber sandstone and the Madison limestone are all saline aquifers: water in the Nugget aquifer has total dissolved solid (TDS) ranging from 5,000 up to 95,700 mg/L with a median of 10,200 mg/L; the TDS of water in the Weber ranged from 3,390 to 72,300 mg/L with a median of 24,600 mg/L; and for the water in Madison TDS ranged from 20,000 to 80,000 (Clarey et al., 2010; Surdam et al., 2007). Because there are no outcrops of the Weber sandstone and the Madison limestone near RSU, groundwater recharge areas are at least 50 miles far away from RSU based on nearest outcrops (Surdam et al., 2009). The relatively high TDS in these saline aquifers at RSU also indicates that recharge of precipitation into them may be at very slow rates.

The target saline water aquifers are the Pennsylvanian Weber sandstone (220 m thick) and Mississippian Madison limestone (~100 m thick) in the eastern flank of RSU. Cap-rock is the Lower Triassic Chugwater siltstone and shale (330-380 m thick), above which more than 1,500 m of Cretaceous marine shale can also be served as cap-rock sealing unit (Surdam et al., 2009).

At the crest of RSU, the Weber sandstone and the Madison Limestone are 1,860 m and 2,250 m below the surface, respectively. Therefore, the advantages of RSU as site for GCS are due to its thick storage formation with a great depth, multiple cap-rock sealing units, and appropriate distance to a large power plant, Jim Bridge (Surdam et al., 2007). The RSU region produces oil and gas from the Nugget, the Phosphoria, the Weber, and the Madison formations (Montgomery, 1996). For detailed geological and hydrogeological information about RSU readers can refer to Surdam et al. (2007 and 2009) and Clarey et al. (2010).

## 3. Methodology

This paper applies the indicator geostatistics (Journel, 1983) and transition probability (Dai et al., 2004) to characterize porosity heterogeneities in saline aquifers (Weber sandstone and Madison limestone), cap-rocks (Chugwater) and surrounding rocks (Phosphoria). Log data from fourteen boreholes were used to retrieve statistical parameters for porosity such as stratum thickness, vertical mean length and volumetric proportion (Table 1-6). Spatial random fields of porosity in four geological formations above were generated by transition probability geostatiscal software (T-PROGS) (Carle, 1999). Once spatial distributions of porosity in these rocks had been acquired, permeability spatial distributions were obtained on the basis of empirical correlation between porosity and permeability. Then, 3D numerical simulations of injection of CO2 into Weber sandstone were conducted with a finite element multiphase flow simulator, FEHM (Zyvoloski et al., 1997).

### 3.1 Indicator Geostatistics

According to density well log, the accumulate probability distributions of porosity are constructed (for example, Figure 4). Three porosity categories are classified for Weber, Chugwater and Madison formations except two categories for Phosphoria formation (see Fig. 4

and Table 1). Each category is treated as a different facies. Using these porosity classifications, i.e. facies, the indicator geostatistics was employed to attain volumetric proportion and vertical mean length for each facies.

Denoting the volumetric proportion of the $k$-th facies as $p_k$, then the sum of volumetric proportion for all facies in any specified formation (for example, the Weber sandstone) should be one, i.e. $\sum_{k=1}^{N} p_k = 1$. Let $X(\mathbf{x})$ be a spatial random variable for porosity ($\phi$), it can be expressed as

$$X(\mathbf{x}) = \sum_{k=1}^{N} I_k(\mathbf{x})\, X_k(\mathbf{x}) \tag{1}$$

where $X_k(\mathbf{x}), k = \overline{1, N}$, represents porosity $X(\mathbf{x})$ of different facies $k$ at location $\mathbf{x}$, and $I_k(\mathbf{x}), k = \overline{1, N}$, is an indicator spatial random variable defined within the domain $\Omega$ as

$$I_k(\mathbf{x}) = \begin{cases} 1, \text{if facies } k \text{ occurs at location } \mathbf{x} \\ 0, \text{otherwise} \end{cases} \tag{2}$$

Following Lu and Zhang (2002) and Ritzi et al. (2004), the composite mean $M_X$ and composite variance $\sigma_X^2$ of porosity are calculated via

$$M_X = \sum_{k=1}^{N} p_k m_k \tag{3}$$

$$\sigma_X^2 = \sum_{k=1}^{N} p_k \sigma_k^2 + \frac{1}{2} \sum_{k=1}^{N} \sum_{i=1}^{N} p_k p_i \, (m_k - m_i)^2 \tag{4}$$

where $m_k$ and $\sigma_k^2$ are the mean and variance of $X_k(\mathbf{x})$ for the facies $k$, respectively. The global means and variances for the Chugwater Phosphoria, Weber and Madison formations are listed in Table 2.

### 3.2 Transition Probability

Taking two locations, $\mathbf{x}$ and $\boldsymbol{\chi}$, separated by a distance vector $\mathbf{h}$, the transition probability $t_{ki}(\mathbf{x}, \boldsymbol{\chi})$ is defined as the conditional probability for the facies $i$ occurring at location $\boldsymbol{\chi}$, given the other facies $k$ occurs at location $\mathbf{x}$:

$$t_{ki}(\mathrm{x}, \chi) = Pr\{I_i(\chi) = 1 | I_k(\mathrm{x}) = 1\} = Pr\{I_i(\chi) = 1 \text{ and } I_k(\mathrm{x}) = 1\} / Pr\{I_k(\mathrm{x}) = 1\} \tag{5}$$

Assuming that both covariance function and transition probability are exponential (Dai et al., 2007a), and that the cross-covariances are negligible (Lu and Zhang, 2002; Dai et al., 2004), the composite covariance function for porosity is expressed as (Dai et al., 2004; Dai et al. 2007b)

$$C_X(\mathbf{h}_\varphi) = \sum_{k=1}^{N} p_k^2 \sigma_k^2 \, e^{-\frac{\mathbf{h}\varphi}{\lambda_k}} + \sum_{k=1}^{N} p_k (1 - p_k) \sigma_k^2 \, e^{-\frac{\mathbf{h}\varphi}{\lambda_\psi}} + \frac{1}{2} \sum_{k=1}^{N} \sum_{i=1}^{N} (m_k - m_i)^2 \, p_k p_i e^{-\frac{\mathbf{h}\varphi}{\lambda_I}} \tag{6}$$

where $\lambda_\psi = \lambda_k \lambda_I / (\lambda_k + \lambda_I)$, $\lambda_k$ and $\lambda_I$ are the integral scale of the facies $k$ and the indicator correlation length, respectively.

After volumetric portions and mean lengths were obtained for porosity of each facies in the geological formations, we use an analytical solution (Dai et al., 2007) to calculate the correlation lengths and integral scales ($\lambda_k$ and $\lambda_I$).

### 3.3 Random Fields Generated by T-PROGS

The borehole data are used to retrieve geostatistical parameters for geological formations in the vertical direction. However, due to scattered boreholes (those data can be obtained)

distributing in research area, the geostatistical parameters in the horizontal direction cannot be directly extracted from available borehole data. We first assume that the horizontal transition probability is the same as the vertical one. This is a reasonable assumption here and for many applications of transition probability (Carle, 1999). We further assume that the horizontal correlation lengths for porosity and permeability in each geological formation are fifty times as large as the vertical ones. With these assumptions, the transition rate matrix were computed through the analytical solution of Dai et al (2007) and the porosity random fields were generated by T-PROGS of Carle (1999) (Fig.5-8). The permeability random fields are mapped from porosity random fields by empirical correlation between porosity and permeability.

**3.4 Numerical simulations using FEHM**

The size of the simulation domain is 16 km (x) × 16 km (y) × 3.6 km (z) (Fig.9). It was discretized into 524,880 tetrahedral nodes with horizontal spacing of 200 m and higher vertical resolution of 10 m in order to capture relative small vertical correlation length for each facies in Madison, Weber, Phosphoria and Chugwater formations. The domain is also tilled to the southeast at an angle of 4° with azimuth of 40° and implicitly includes 2 km overburden rock above its top. There are sixteen injection wells located about 40 to 45 m above the bottom of the Weber sandstone in the center of the domain. In order to reduce saline aquifer pressure and increase storage capacity for $CO_2$, four production wells are designed at the top of the Weber sandstone near each corner of the domain (Fig.9). Injection of CO2 into the Weber sandstone is with fixed temperature (45 °C) and constant injecting pressures, which are equivalent to 75% of lithostatic pressures. The production wells pump brines only when they sense the fluid pressures above the values of steady-state flow field before injection of $CO_2$.

**Boundary Conditions** The bottom of the simulation domain is no flow boundary. The top and four lateral boundaries are set as specified pressure boundaries. Constant temperatures are held at the top (63 °C) and bottom (158 °C) of the domain, which is equivalent to a specified geothermal gradient from the bottom up (Fig.10).

**Initial Conditions** The steady-state groundwater flow temperature and pressure fields are used as initial conditions for all simulations in this study. Initial CO2 fractions in injection well nodes are set as zero.

**Relative Permeability** The linear relative permeability model (equation 7 and 8) is used for all simulations in this study (Fig.11). It prescribes the residual saturations ($\theta_r$) of 0.10 and maximum saturation ($\theta_S$) of 0.90 for both brine ($w$) and $CO_2$.

$$k_{rw} = \begin{cases} 0, & \theta_w \le \theta_{wr} \\ \dfrac{\theta_w - \theta_{wr}}{\theta_{ws} - \theta_{wr}}, & \theta_{wr} \le \theta_w \le \theta_{ws} \\ 1, & \theta_w \ge \theta_{ws} \end{cases} \tag{7}$$

$$k_{rCO_2} = \begin{cases} 0, & \theta_{CO_2} \le \theta_{CO_2 r} \\ \dfrac{\theta_{CO_2} - \theta_{CO_2 r}}{\theta_{CO_2 s} - \theta_{CO_2 r}}, & \theta_{CO_2 r} \le \theta_{CO_2} \le \theta_{CO_2 s} \\ 1, & \theta \ge \theta_{CO_2 s} \end{cases} \tag{8}$$

**Density and Solubility of Supercritical $CO_2$ and Brine** FEHM incorporates the $CO_2$ density model (Duan et al., 2008) and solubility model of $CO_2$ in brine (Duan et al., 2006) into its $CO_2$ module. Combining with its thermodynamic module, FEHM can calculate the density, viscosity, solubility of $CO_2$ with changing temperature and pressure.

**Porosity and Permeability** The porosity parameters are obtained from geostatistics of borehole log data (Table 1). The permeability parameters are mapped from porosity through

empirical correlations between porosity and permeability. The permeability of the Weber sandstone is calculated by a linear correlation equation ($logk = 0.1937\phi - 1.2911$, where $k$ is permeability in milidarcy (mD), $\phi$ is porosity in %), which is by regression analysis of data of the Weber Sandstone and its equivalent Tensleep Sandstone from the Wind River , the Greater Green River, and the Big Horn Basins in Wyoming (Nelson & Kibler, 2003). Fig. 12 shows the parameters used in simulations (black solid circles), and the other two empirical correlations for sandstone of Bethke (1985) and Bense et al. (2006) for the purpose of comparison. The linear correlation is pretty good with correlation coefficient of $R^2$ = 0.78. The permeability of the shale and clayed sandstone is a much complex function of porosity, clay content, effective stress and diagenesis (Yang & Apline, 2010). High quality data of porosity and permeability for shale and mudstone is relatively rare (Neuzil, 1994). A simple linear regression relationship cannot capture realistic relationship between porosity and permeability. We decided to use the empirical correlation of Yang & Apline (2010) below to compute the vertical permeability of the cap-rock, Chugwater with an assumption of clay content of 25%.

$$lnk = -69.59 - 26.79C + 44.07C^{0.5} + (-53.61 - 80.03C + 132.78C^{0.5})e + (86.61 + 81.91C - 163.61C^{0.5})e^{0.5} \quad (9)$$

Where $e=\phi/(1-\phi)$, $e$ is void ratio and $\phi$ the porosity, $k$ is vertical permeability in unit of $m^2$, and $C$ is clay content in percent. Fig.13 shows the porosity and permeability used in simulations (black solid circles). The simple linear regression (black solid line) cannot account of four to six orders of magnitude of variation in permeability corresponding to each value of porosity. For the permeability in the Phosphoria and the Madison (Table 1), an empirical power law between porosity and permeability below were used (Bernabe et al., 2003):

$$k = a \times \phi^b \quad (10)$$

where $a = 1.5\times10^{-12}$ $m^2$ and $b = 3.0$.

Permeabilities for all facies and all rocks are prescribed as isotropic except for cap-rock, Chugwater formation with anisotropy ratio of 10 (horizontal permeability is ten times larger than vertical one). Density of all rocks is fixed at 2650 $kg/m^3$. Geomechanical effects due to fluid pressure build-up from injection of $CO_2$ are not considered in this paper though they are important for monitoring leakage of $CO_2$ from reactivation of pre-existing faults and faulting cap-rocks. Neither are the geochemical reactions among supercritical $CO_2$, brine and rocks.

## 4. Results

The results presented in this paper are based on more than ten simulations. However, the most plots are based on the simulation run, perm-6666-p75 unless a specification is given. The number 6666 in the name of simulation run denotes the realization number from the left to right for the Chugwater, the Phophoria, the Weber and the Madison formations. All simulation runs are named in the same way in this study.

### 4.1 Heterogeneities in Storage Formation and Cap-rock in RSU, Wyoming

Ten realizations for random porosity fields are generated for each geological formation (Madison, Weber, Phosphoria, and Chugwater) by T-PROGS using parameters listed in Table 1-2. With empirical correlations between porosity and permeability, the permeability random fields are retrieved from the random porosity fields (Table 6 and Fig.5-8).

Applying equations (3) and (4), we computed the global means and global variances for porosity and permeability in each geological formation. The porosity global means are 5.9%, 4.5%, 4.8%, and 6.1% for the Chugwater, Phosphoria, Weber and Madison formations, respectively; the porosity global variances are 28.7, 13.8, 16.1 and 30.5 respectively for the Chugwater, Phosphoria, Weber and Madison formations (Table 2). The global mean of the

porosity can be treated as an upscaled or effective porosity for each formation. The result reveals that the storage formations (Weber and Madison) do not have effective pore space as much as what ones expected before, and on other hand, that the cap-rock (Chugwater) may have relatively large storage capacity for fluids due to relatively high porosity (about 6%). The global variances display relatively large heterogeneity in porosities within each formation. From Fig.5-8 the porosity random fields show the facies of high porosity (faicies 3 for Chugwater, Weber and Madison; faicies 2 for Phosphoria) usually don't connect each other. However, the facies of high porosity normally link the facies of mediate porosity. This means that relatively fast flow paths will go through facies 2 and 3. In cap-rock, the Chugwater formation, all facies show layer-like distribution in space while in the Phosphoria and Madison formations the facies of mediate and high porosity display relatively large vertical extension. The facies in the Weber formation show spatial distribution features between the former and the latter both in vertical and horizontal directions.

The global means and global variances of permeability are calculated and listed in Table 2. It shows the cap-rock has very low effective permeability value of log$k$ = -19.34 (equivalent to 0.000045 milidarcy) with a relatively small global variance of 1.38 (log10 based). The Weber Sandstone has relatively large effective permeability value of log$k$ = -16.46 (equivalent to 0.035 milidarcy) with the smallest global variance of 0.69 among the four formations. The Phosphoria formation exhibits the largest global variance for permeability, which is consistent with its transition features having different petrology. The second largest global variance for permeability (2.35) for the Madison limestone is also compatible with its complex features of karstification and dolomitization.

These characterized spatial heterogeneities for porosity and permeability are then incorporated into our model to simulate supercritical $CO_2$-brine multiphase flow with injection of $CO_2$ for fifty years using the simulator of FEHM.

### 4.2 Growth and Migration of $CO_2$ Plume

In this study we simulate injecting supercritical $CO_2$ into Weber sandstone for fifty years. Since the injection starts, the fluid pressure increases rapidly (Fig.14); the $CO_2$ plume begins to form, migrate and grow (Fig.15); the temperature around injection wells decreases because the temperature of the injected $CO_2$ is lower than ambient brine (Fig.16). At the end of fifty years of injection, supercritical $CO_2$ plumes expand and gradually move away from the injection wells (Fig.17). Although the fluid pressure field has been perturbed since the beginning of the injection of $CO_2$ (Fig.14b), the individual supercritical $CO_2$ plumes formed by each injection well still have not merged together (Fig. 15 and 17). The contour of the supercritical $CO_2$ fraction (Fig.17) clearly demonstrates the shape and interior structure of the plume while the contour of the dissolved $CO_2$ fraction (Fig.15) displays the maximum size and outside boundary that the $CO_2$ plume can reach.

**Fluid Pressure Field** The fluid pressure field has been full changed since injection of $CO_2$ (Fig.14). However, the pressures at the upper and left corners are not affected. Pressure interference among different injection wells starts very early, before less than one year of injection of $CO_2$. The whole fluid pressure field in horizontal profile showed in Fig.14 seems reach a quasi-steady state since injection of $CO_2$ for about ten years. It implies that the changes in fluid pressure for the following forty years will probably occur most in vertical direction, and the increasing fluid pressure will gradually propagate into cap-rock. As shown in Fig.19, the fluid pressure at the bottom of the Chugwater increases about 20 MPa (Fig.19b) comparing to the

unperturbed fluid pressure field (Fig.19a). Close to the top of the Chugwater formation, the fluid pressure increases about 5 MPa.

**Temperature Field** The temperature field has not been full influenced by injection of $CO_2$ except the very small areas around the injection wells, where a temperature gradient formed: in the center of injection wells it is equal to the injected temperature of 45 °C and toward outside it quickly rises to the ambient temperature (Fig.16). The larger the $CO_2$ plume grows, the broader the area with lowered temperature becomes.

**Growth and Migration of $CO_2$ Plume** Since the injection started, the $CO_2$ plume begins to form and further grows large and large (Fig.15, 17, 18). The $CO_2$ plumes don't grow uniformly in horizontal direction. At the end of fifty years of injection the sixteen $CO_2$ plumes have their different size. It implies that different wells have very different injectivity. Fig.17 shows the $CO_2$ plumes have preferential direction to grow and migrate. The largest $CO_2$ plume in left side of the Fig.17 exhibits an irregular shape and intensely spreads to the left, where a pumping well (Fig.9) is located nearby and a relative high-porosity facies exists (Fig.20). The migration direction of $CO_2$ plume is signified by its advance front of dissolved $CO_2$ (Fig.15 and Fig.18). In vertical profiles (Fig 17a, Fig.18 and Fig.21a), the $CO_2$ plume at the lower right side is migrating far away to the deep with a long hand while the $CO_2$ plume at the upper left side is migrating to the shallow with a very short front. Fig.17a and Fig.18 also reveal that the $CO_2$ plume at the upper left side penetrates into the Madison limestone, a formation below the Weber Sandstone. In fact, the fronts of the dissolved $CO_2$ for many $CO_2$ plumes advance into the lower Madison formation (Fig.18). As expected, all $CO_2$ plumes show their expansion at top even they have different preferential directions to spread due to buoyancy. Furthermore, all $CO_2$ plumes have not passed the domain boundary for fifty years of injection.

### 4.3 Injectivity and Production of Wells

Due to constant injection pressure used in our simulations, the injection rate changes with time in each injection well. However, the wells with high injectivity reach their steady-state injection rate quickly within about three years (well 11_5, well 5_11) while the wells with low injectivity take about four to five years (even longer) to approach their steady-state injection rates (well 7_7, well 11_7) (Fig.26). The well with lowest injectivity corresponds to the $CO_2$ plume of smallest size.

The pumping wells all experience a rapid growth of production rate for ten years except well 14_14 for only five years (Fig.27). After the rapid growth period, all pumping wells enter a phase of steady and slow increasing pumping rate. The well 2_14 has the largest pumping rate while the well 2_2 has the smallest rate. The larger the pumping rate for a well, the higher the fluid pressure for the well to release.

### 4.4 Storage Capacity and Leakage

Large variation in total amount of $CO_2$ injected for fifty years has been revealed in cases of different combinations of realizations of random fields of porosity and permeability for the Chugwater, the Phosphoria, the Weber and the Madison formations (Table 3 and Fig.26). The largest amount of injected $CO_2$ achieves in the simulation run perm-6444-p75 with 693 Mt for 50 years of injection while the smallest amount of injected $CO_2$ is 426 Mt in the simulation run perm-9909-p75. The average amount of $CO_2$ injected for fifty year over forty two simulation runs is 559 ± 22 Mt at 95% confidence interval, with a coefficient of variation of 12.8% and the associated brine production is on an average of 478 ± 24 Mt at 95% confidence interval, with a coefficient of variation of 16.5%. The average ratio of the amount of injected $CO_2$ to the produced brine is 1.18. This ratio indicates the production wells are necessary design to reduce

fluid pressure and enhance storage capacity for $CO_2$ sequestration. The total mass of injected $CO_2$ and produced brine both linearly increase with time after one year of injection (Fig.28). This manifests that the $CO_2$ injection rate in the whole domain reaches steady state as quickly as one year even though the individual injection well achieves its steady state at different time (Fig.26).

Storage capacity for RSU is estimated on the basis of numerical simulation results above. We assume that the 3D simulation domain is a representative element, whose heterogeneity structure is identical to that of the whole RSU. Therefore, once the volumes of the saline aquifers in the simulation domain ($V_{simu}$) and in the whole RSU ($V_{RSU}$) are known, the storage capacity ($C$) can be calculated by following equation:

$$C = \frac{V_{RSU}}{V_{simu}} \times M_{CO2} \tag{11}$$

where $M_{CO2}$ is the average mass of $CO_2$ injected into saline aquifers in the simulation domain for fifty years. The uncertainty of estimating storage capacity is considered to be equivalent to the uncertainty in the mass of $CO_2$ injected into the saline aquifers in the simulation domain. The estimation results are given in Table 4, where the volume of the saline aquifers (Weber Sandstone) in the simulation domain is calculated by its grid generator while the volume of the saline aquifers in the whole RSU is computed according to an Earth-Vision model. The storage capacity for $CO_2$ sequestration in RSU is 6614 ± 256 Mt associated with 5655 ± 282 Mt produced brine at 95% confidence interval. This estimation is about 36% ± 1% of the previous one made by Surdam & Jiao (2007), who assumed a homogeneous and isotropic saline aquifer (Weber Sandstone) at RSU and the $CO_2$ plume uniformly expanding in the RSU-covered area of 1300 $mile^2$.

Table 5 shows how much amount of $CO_2$ leaks from the storage formation (Weber sandstone) into the Phosphoria and the Chugwater formations. The total amount of leaked $CO_2$ is about 2%

to 20%, with an average 12%, of the total amount of the injected $CO_2$. If only considering $CO_2$ leaked into the Chugwater, it is less than 0.6% of total amount of the injected $CO_2$. There is no $CO_2$ leaking into the formations above the Chugwater for fifty years of injection. Neither does any $CO_2$ plume move out of the boundaries of the simulation domain although there are less than 1% dissolved CO2 leaving the domain with the brine.

## 5. Discussion

### 5.1 On Representativeness of Limited Borehole data

Because limited borehole data are used to retrieve geostatistical parameters describing the spatial heterogeneities of porosity and permeability in geological formations (Chugwater, Phosphoria, Weber and Madison) at RSU, a question may reasonably rises how representative the limited borehole data used are. On the basis of the indicator geostatistics and transition probability method used here, the vertical heterogeneities are full captured better than the horizontal ones. Combined with geological setting of the geological formations, we believe the heterogeneities in the Weber and the Chugwater are defined far effectively and better than those within the Phosphoria and the Madison because of their regional geological continuities. The Phosphoria is much complex due to transition in lithofacies. So is the Madison due to karstification and dolomitization. With limited data available, we preliminarily constrain the spatial heterogeneities in storage formations and cap-rocks and address their potential influences on CGS at RSU in order to assess the uncertainty and risk associated with CGS. As soon as site characterization data (geological and geophysical) are available at RSU, we can easily incorporate them into our present model.

The other limit of the borehole data used in this study is that we didn't consider the heterogeneity resulted from geological structure such as deformation bands, faults and fractures.

In order to incorporate these types of heterogeneity, a detailed 3D structural mapping is needed at RSU. This is beyond the scope of this paper.

### 5.2 Classification of Facies in the Geological Formations

The classification of facies in the geological formation is somehow subjective based on the porosity histograms and cumulative probability curves (Fig.4 and Table 1) because the detailed lithological data in borehole log are not available for us. However, the identified categories indeed reflect major features of porosity distribution in each geological formation. For example, for the Weber Sandstone (Fig.4), the cut-off ranges for low, mediate and high porosity facies are $\leq$ 5.0, 5.0-15.0 and >15.0, respectively, and the corresponding cumulative probability ranges are 0-57.98%, 57.98%-94.17%, and 94.17%-100%, respectively. The points (5.0, 57.98%) and (15.0, 94.17%) are turning points at which the cumulative probability curve changes its slope and histogram shows different frequency trends. These trends or changes exhibit the features of porosity distribution in space.

### 5.3 Density Profiles of Brine and $CO_2$ and Convection

During fifty year of $CO_2$ injection, brine density continues to increase due to dissolution of $CO_2$ into it. Fig. 22 shows at the end of fifty year of $CO_2$ injection, the density of brine around injection wells is much larger than ambient brine, especially the largest in the injection nodes. Because of cap-rock hindrance of Chugwater formation, density anomaly was confined below the top of Chugwater. On the other hand, while checking the density profile of supercritical $CO_2$ (Fig.23), the largest density anomalies appeared in injection nodes owning to lower injection temperature (45 °C) and higher fluid pressure from injection. Similarly, the density anomaly of supercritical $CO_2$ was limited below the top of Chugwater. However, compared with brine density profile (Fig.22), the density anomaly of supercritical $CO_2$ propagated much deeper into Madison limestone and bedrock. This is because the injection pressure pushed supercritical $CO_2$

down to the bottom in addition to effect of density contrast between hot brine and cold supercritical $CO_2$. In order to further examine density contrast hot brine and cold supercritical $CO_2$, the contours of the density ratio of the supercritical $CO_2$ to brine was plotted in Fig.24. Although the whole pattern of the density ratio is similar to that of the density of supercritical $CO_2$ (Fig.23), the Fig 24 clearly shows that the densities of the supercritical $CO_2$ are almost the same as those of ambient brine in the injection nodes. This has remarkable implications for stability of the supercritical $CO_2$ injected into a low-salinity aquifer more than 3.5 km deep in subsurface. There may be a range of injection depth, temperature and pressure, within which the supercritical $CO_2$ plume would not move upward for a long time due to almost identical densities between brine and $CO_2$ before thermal equilibrium reaches. To our knowledge, previous simulations of $CO_2$ sequestration into saline aquifers were almost performed at depth of shallower than 3.5 km. It could be the reason why an optimal depth-temperature-pressure window has not been found for $CO_2$ sequestration.

Thermal convection of fluid flow in subsurface porous media can be evaluated with Rayleigh number (Ra). The minimum critical value of the Raleigh number is $4\pi^2$ for onset of convection

$$Ra = \frac{\alpha_f g \rho_f^2 c_{pf} k b (T_1 - T_0)}{\mu \lambda_m} \tag{12}$$

(Turcotte, and Schubert, 2002). Taking fluid parameters listed in table 6, a Rayleigh number is calculated equal to 0.34, which is far less than the minimum critical value of $4\pi^2$. Therefore, even the brine density profile is upside down in the simulation domain (Fig.25), it is still impossible to generate fluid convection. If considering heterogeneities in porosity and permeability within Weber sandstone, thermal convection of brine and supercritical $CO_2$ flow may rarely occur due to impedance of low permeability facies.

### 5.4 On Regional Groundwater Flow

The regional groundwater flow is rarely known in Weber Sandstone at RSU. The only information available for us is the report of Clarey et al. (2010), in which on the basis of the simulated potentiometric surfaces in the Weber sandstone aquifer, they inferred the direction of regional groundwater flows in the Weber is generally away from RSU to the nearby basins, but the flow rate is not well defined. According to high TDS in the Weber saline aquifer (> 10,000 mg/L), distant outcrop area for recharge (at least 50 miles far away) and thick confining layers above it (>1,500 m) (Surdam and Jiao, 2007; Surdam et al., 2009), we consider the regional groundwater flow maybe very slow and be neglected at RSU. On the other hand, Even if there is a very slow regional groundwater flow at RSU in direction of down-uplift as mentioned by Clarey et al. (2010), the very slow regional groundwater flow will opposite migration direction of the $CO_2$ plume due to buoyancy, and reduce migration rate of the $CO_2$ plume. MacMinn et al. (2010) confirmed theoretically that a gentle down-slope flow actually makes storage efficiency increase several times because of capillary trapping compared to that for a horizontal saline aquifer. There are four possibilities: first, the buoyancy of $CO_2$ plume overcomes the potential of the regional groundwater flow and the $CO_2$ plume migrates upward to the crest of RSU at slower rate; second, the buoyancy of $CO_2$ plume cancels the potential of the regional groundwater flow and the $CO_2$ plume stay at the injection site; third, the buoyancy of $CO_2$ plume is less than the potential of the regional groundwater flow and the $CO_2$ plume migrates downward to the depth of the nearby basin. Due to increasing temperature with depth, the buoyancy of the $CO_2$ plume will increase due to increase in temperature. At a certain depth, the $CO_2$ plume would stay still due to the buoyancy large enough to cancel the potential of the regional groundwater flow. The fourth, the potential of the regional groundwater flow is large enough to drive $CO_2$ plume all the

way to its discharged area. Whatever one of the first three possibilities is, there will be no special risk associated with migration of the $CO_2$ plume. The fourth possibility is not realistic based on geological setting though it may cause huge risk of leakage of $CO_2$. Further simulations will be needed to address CGS into the Weber sandstone under regional groundwater flow at RSU.

**5.5 Effects of Heterogeneity on Well Injectivity and Production**

Determining the right locations of the injection wells is crucial for $CO_2$ sequestration. If an injection well is erroneously located in a low-permeable zone (facies) without high-permeability zone nearby such as well 11-7 and 7-7 in Fig.15 and Fig.26, it results in very low $CO_2$ injectivity in these wells (more than 10 times smaller compared to high-injectivity wells); it causes to increase costs to improve injectivity in such situation, even failure of a project. Heterogeneity of porosity and permeability in geological formations requests ones to make a detailed characterization of storage formation before an injection well is located.

Because of the fixed injection pressures in our simulations, $CO_2$ injection rates change with time. At the beginning of injection, the injection rates dramatically rise to a peak for each injection well (not shown here due to very short time scale); then gradually decrease to a quasi steady-state rate within first five years of $CO_2$ injection (Fig.26), which are kept to the end of the $CO_2$ injection. This typical evolution curve for injection rate is different than that predicted from an analytical solution for well injectivity in an infinite, homogeneous and isotropic aquifer (Stauffer et al., 2009). The latter forecasts the injection rates would continually decrease with time when the injection pressure is fixed. However, the quasi steady-state injection rates after 5 years of injection in our simulation domain are consistent with those for a bounded domain with constant-pressure at outer boundaries (Matthew & Russel, 1967).

Fig.26 also reveals that the different wells have different injectivity even if some wells are located in the same facies (comparing Fig.21 with Fig.20). The wells along diagonal line (well 5-

5, well 7-7, well 9-9, and well 11-11) in Fig.26 correspond to the wells with the same arrangement in Fig.18. Comparing Fig. 18 with Fig.20 and referring to the well injectivity in Fig.26, it is clear that the wells with high injectivity are located in or nearby a facies with high porosity and permeability (due to correlation between porosity and permeability). This conforms to the trend predicted by the analytical solution. The wells within the same facies but with different injectivity are due to influence from different neighbor facies and interference between injection wells and production wells. When a production well can effectively reduce the fluid pressure in its neighbor area, the injection wells in the neighbor area inject more $CO_2$, such as injection well 5_11 and 7_11 close to pumping well 2_14 (Fig.21 and 26). The steady-state injection rates under constant injection pressure are maintained by stable reduction in fluid pressure through production wells.

The four pumping wells sense different fluid pressures at different locations and thus have different production rates (Fig.27). Comparing porosity field (Fig.20) with well locations (Fig.9) and production rates (Fig.27), it is shown that the wells within or near a high-porosity facies, for example, well 2_2 and 14_14, see lower fluid pressure due to rapid dissipation of pressure through the high-porosity facies and have lower production rates; the wells within a low-porosity facies, for example, well 2_14 and 14_2, feel higher fluid pressure and have higher production rates.

Therefore, locating injection wells and production wells within and nearby a facies with high-porosity and permeability is crucial for design of $CO_2$ geological sequestration.

**5.6 Effects of Heterogeneity on Pressure Buildup and $CO_2$ Plume Migration**

After injection of $CO_2$ from a well for an enough long time, the pressure buildup in a homogeneous and isotropic saline aquifer with constant-pressure outer boundaries, can reach a steady-state (Matthew & Russel, 1967). The steady-state pressure is close to the difference

between the injection pressure and the outer boundary pressure. The maximum pressure buildup occurs in the injection well. This is roughly consistent with our numerical simulation results after 10 years of injection (Fig.14). However, in our study where heterogeneities in porosity and permeability are considered, the high-porosity facies can be thought as many small regions bounded by the boundary between high-porosity and low-porosity facies. When $CO_2$ plume approaches to the boundary, pressure buildup increases much due to low-porosity facies and the plume migration is also slowed down and confined by the low-porosity facies (Fig. 18 and 20). Zhou et al. (2009) showed that at such boundaries, the enhanced pressure buildup caused increasing vertical leakage of brine from storage formation through cap-rock to upper aquifer in order to make pressure dissipate. Based on our simulations, the vertical leakage of brine or $CO_2$ is also constrained by contrast in permeability at the lateral boundary and vertical boundary. If the lower permeability existed at vertical boundary, the $CO_2$ plume and brine would prefer lateral movement rather than vertical migration (Fig.18 and 21).

Using parameters listed in Table 11 to calculate the influence radius (equation 13) (Bear, 1979; Vilarrasa et al., 2010), it is shown that for the brine $R_{in}$ is 7.231 km, but for the $CO_2$ fluid $R_{in}$ is larger than 10 km. The influence radius tells ones that when a pressure buildup appears in an infinite homogeneous and isotropic aquifer due to injection or pumping, how far the aquifer pressure field is influenced in the radial distance from the well.

$$R_{in} = \sqrt{\frac{2.25 k \rho_f g t}{\mu_f S_s}} \tag{13}$$

where $\rho_f$ is fluid density (kg/m$^3$), $\mu_f$ viscosity of fluid (Pa·s) and $g$ the gravitational acceleration (m/s$^2$), $k$ permeability (m$^2$) and $t$ is time (s). From Fig.14 and 19 in a heterogeneous field, the

radii for fluid pressure perturbation due to 1year, 10 years and up to 50 years of injection are basically consistent with the trend predicted by the equation (13) although there are complex patterns for pressure distribution and more rapid pressure buildup due to low-permeability facies distributed in the domain. More accurate prediction of pressure buildup and $CO_2$ plume migration needs numerical simulations involving spatial heterogeneity of porosity and permeability.

### 5.7 Effects of Heterogeneity on Storage Capacity and Leakage of $CO_2$

The design of fifty years of injection is to simulate $CO_2$ sequestration corresponding to a typical life time of a coal-fired power plant in the North America (Stauffer et al., 2009b). The choice of sixteen injection wells and four production wells is to intend exploration of maximum storage capacity under a scheme of reduction in pressure buildup by pumping brine. The injection pressure with about 75% lithostatic pressure is comparable to the maximum sustainable injection pressure estimated by Rutqvist et al. (2007), who used analysis of coupled fluid flow and geomechanical fault-slip under conditions of hypothetical compression and extension stress. Because the storage capacity is mainly controlled by heterogeneities of porosity and permeability in storage formation and cap-rock, numerical simulation is selected in this study in order to incorporate the heterogeneous fields.

The heterogeneities give the major contributions to the uncertainty in storage capacity. The box plot of the injected and leaked $CO_2$ in Fig.29 demonstrates a large range for the injected $CO_2$ with median of 564.4 Mt. Its probability distribution is shown in Fig.30a and b. The Quantile-Quantile (Q-Q) plot (Fig.30c) reveals it follows a normal distribution with a mean of 559 Mt and a standard deviation of 72 Mt (Table 3). The Lilliefors' normality test confirm the inference of the Q-Q plot, in which the maximum distance of 0.096 between the empirical cumulate

distribution function (CDF) of the simulation data and theoretical CDF of the normal distribution is smaller than the critical value of 0.124 given a probability value of 0.1. This relatively well defined uncertainty in the injected $CO_2$ provides a reliable precondition for estimation of storage capacity for RSU.

True spatial distribution of different lithofacies of the Phosphoria formation at RSU is much uncertain to some degree for us at the time of collecting data and performing numerical simulation, due to transition from chert- and phosphorite-bearing black shale in the west to the limestone and dolostone in the east. This uncertainty causes large uncertainties in determining porosity and permeability fields in Phosphoria formation and an uncertainty in judging the Phosphoria as a storage formation or a cap-rock in whole RSU, which further results in an additional uncertainty in evaluation of storage capacity of $CO_2$ at RSU.

Potential effects of faults and fracture on $CO_2$ sequestration at RSU are ignored here because most faults on surface do not extend to the depth where $CO_2$ is injected and the blind thrust fault in the western flank of RSU is a sealed one (see geological setting). The other reason for this is that we don't know the on-site stress field at RSU and cannot do further practical analysis of fault effects without principle stresses.

With different combinations of random porosity and permeability fields, the coefficient of variation of $CO_2$ leakage is as large as 38%, and 83% respectively for $CO_2$ leaked into the Phosphoria and the Chugwater formations, and 39% for total $CO_2$ leakage. The probability distributions of the leaked $CO_2$ into the Phosphoria and into the Chugwater follow a normal distribution (Fig.31) and a log normal distribution (Fig.32), respectively. Their corresponding Q-Q plots support this finding (Fig.31c and Fig.32c), which is consistent with the results of Lilliefors tests. Such uncertainties in $CO_2$ leakage are mainly contributed by heterogeneities of

porosity and permeability in the Weber, the Phosphoria and the Chugwater formations. These variations also indicate heterogeneity in porosity and permeability fields may create fast paths or channels for $CO_2$ migration. For instance, the large amount of $CO_2$ leaking from the Weber into the Phosphoria for runs perm-6444-p75 and perm-6666-p75. If such channels connected with faults, the risk of $CO_2$ leakage into upper freshwater aquifers or up to the surface would significantly increases when the faults are activated by increasing fluid pressure.

The injected $CO_2$ is neither correlated with the $CO_2$ leaked into the Phosphoria, nor with that into the Chugwater (Fig.33a). However, there is a weak correlation with correlation coefficient of 0.7 between the $CO_2$ leaked into the Phosphporia and that into the Chugwater (Fig.33b). It indicates that to some degree the high-porosity facices in the Phosphoria indeed connect with those in the Chugwaterat at a statistically significant level. This will raise risk of $CO_2$ leakage into the upper aquifers through the Chugwater. On other hand, the strong correlation between the injected $CO_2$ and the produced brine (Fig.34) emphasizes the importance of release of pressure by pumping brine.

## 6. Conclusions and future research

Based on our numerical simulation of $CO_2$ geological sequestration at RSU, Wyoming, several conclusions can be drawn blow:

(1) Based on indicator geostatistcs, transition probability and Markov chain model, the porosity heterogeneities in storage formation (the Weber sandstone and the Madison limestone) and cap-rocks (the Phosphoria and Chugwater formations) are descripted with global variances of 16, 31, 14 and 29 for the Weber, Madison, Phosphoria and Chugwater, respectively.

(2) The permeability random fields are mapped according to empirical relationship between porosity and permeability. The global variances of log permeability are 0.69, 2.35, 3.54 and 1.38 for the Weber, Madison, Phosphoria and Chugwater, respectively.

(3) Multiphase flow simulation involving field-scale heterogeneity of porosity and permeability in storage formation and cap-rocks at RSU reveals that well injectivity depends on local permeability distribution in storage formation, and thus injection well design seriously rely on it too. Under the given design of injection, the maximum injection rate can be up to 30 kg/s for decades.

(4) Brine production is a necessary method to reduce pressure buildup in the storage formation and enhance storage capacity. Brine production rates increase with time and positively correlate with the amount of injected $CO_2$.

(5) The spatial distribution of liquid pressure buildup in the storage formation is controlled by spatial heterogeneity of porosity and permeability, injection pressure, location of injection and production wells and types of boundary (close or open). This has potential importance on hydraulic fracturing of the reservoir rock, reactivation of pre-existing faults and the integrity of the cap-rock;

(6) The density profiles show that the density of $CO_2$ injected below 3 km is close to that of the ambient brine with given geothermal gradient and brine concentration, which indicates $CO_2$ plume first can sink to the deep before reaching thermal equilibrium with brine.

(7) $CO_2$ leakage from storage formation into cap-rock is related to connectivity of high-permeability facies in storage formation and cap-rocks. No correlation is found between the injected $CO_2$ and $CO_2$ leakage. However, the leaked $CO_2$ into the Phosphoria is positively correlated with that into the Chugwater. The $CO_2$ leaked into Phosphoria

displays the normal distribution, but $CO_2$ leaked into the Chugwater shows the log normal distribution.

(8) Injected $CO_2$ follows the normal distribution. At 95% confidence interval, the $CO_2$ storage capacity at RSU is estimated to be 6614 ± 256 Mt, which is about 36% of previous estimation relying on homogeneous and isotropic storage formation and cap-rocks.

Future research will include the potential regional ground flow into our simulations. When in situ stress field is available at RSU, geomechanical effects will be coupled with multiphase flow in our modeling. Geochemical reaction in the sandstone storage formation is another area for further study.

**Acknowledgements** This study is funded by US DOE and the State of Wyoming. Dr. Carl Gable and Terry Miller set up finite element grids; Drs. George Zyvoloski, Zora Dash and Rajesh Pawar helped in FEHM.

## References


Ambrose, W.A., Lakshminarasimhan, S., Holtz, M.H., Nunez-Lopez, V., Hovorka, S.D., and Duncan, I., 2008. Geologic factors controlling $CO_2$ storage capacity and performance: case studies based on experience with heterogeneity in oil and gas reservoirs applied to $CO_2$ storage. Environmental Geology 54, 1619-1633.

Bachu, S., Gunter, W.D., and Perkins, E.H., 1994. Aquifer disposal of $CO_2$: hydrodynamics and mineral trapping. Energy Conversion and Management 35, 269-279.

Bachu, S. and J.J. adams, 2003. Sequestration of $CO_2$ in geological media in response to climate change: capacity of deep saline aquifers to sequester $CO_2$ in solution. Energy Conversion and Management 44, 3151-3175.

Bachu, S., Bonijoly, D., Bradshaw, J., Burruss, R., Holloway, S., Christensen, N.P., Mathiassen, O.M., 2007. $CO_2$ storage capacity estimation: Methodology and Gaps. International Journal of Greenhouse Gas Control 1, 430-443.

Bernabe, Y., Mok, U., and Evans, B., 2003. Permeability-porosity relationships in rock subjected to various evolution processes. Pure and Applied Geophysics 160, 937-960.

Bear, J., 1979. *Hydraulics of Groundwater*, McGraw-Hill, New York, 569p

Benson, S.M. and Cole, D.R., 2008. $CO_2$ sequestration in deep sedimentary formations. Elements 4, 325-331.

Bensen, V.F. and Person, M.A., 2006. Faults as conduit-barrier systems to fluid flow in siliciclastic sedimentary aquifers. Water Resources Research 42, W05421, doi:10.1029/ 2005WR004480.

Bethke, C.M., 1985. A numerical model of compaction-driven groundwater flow and heat transfer and its application to the paleohydrology of intracratonic sedimentary basin. Journal of Geophysical Research 90, 6817-6828.

Bickle, M.J., 2009. Geological carbon storage. Nature Geosciences 2, 815-818.

Bradshaw, J., Bachu, S., Bonijoly, Buruss, R., Holloway, S., Christensen, N.P., and Mathiassen, O.M., 2007. $CO_2$ storage capacity estimation: Issues and development of standards. International Journal of Greenhouse Gas Control 1, 62-68.

CSLF Task Force, 2008. Comparison between methodologies recommended for estimation of $CO_2$ storage capacity in geological media. Phase III report, by CSLF Task Force on $CO_2$ Storage Capacity Estimation and the USDOE capacity and Fairways Subgroup of the Regional Carbon Sequestration Partnerships Program.

Cavanagh, A.J., Haszeldine, R.S. and Blunt, M.J., 2010. Open or Closed? A discussion of the mistaken assumptions in the Economides pressure analysis of carbon sequestration. Journal of Petroleum Science and Engineering 74, 107-110.

Carle, S.E., 1999. T-PROGS: Transitional Probability Geostatistical Software Users' Guide. University of California, Davis, 1999.

Carroll, S., Hao, Y., and Aines, R, 2010. Geochemical detection of carbon dioxide in dilute aquifers. Geochemical Transactions 10, doi:10.1186/1467-4866-10-4.

Celia, M.A., J.M. Nordbotten, B. Court, M. Dobossy, and S. Bachu, 2011. Field-scale application of a semi-analytical model for estimation of $CO_2$ and brine leakage along old wells. International Journal of Greenhouse Gas Control 5(2), 257-269, doi:10.1016/ j.ijggc.2010.10.005.

Celia, M.A. and J.M. Nordbotten, 2009. Practical Modeling Approaches for Geological Storage of Carbon Dioxide. Groundwater, 47(5), 627-638.

Clarey, K.E., T. Bartos, D. Copeland, L.L. Hallberg, M.L. Clark, and M.L. Thompson, 2010. Available groundwater determination - Technical Memorandum. WWDC Green River Basin Water Plan II – Groundwater study, Level I (2007–2009).

Corey, J.W., R. Svec, R. Grigg, J. Zhang and W. Crow, 2010. Experimental investigation of wellbore integrity and CO2-brine flow along the casing-cement microannulus. International Journal of Greenhouse Gas Control 4, 272-282.

Dai, Z., Ritzi, R.W., Huang, C., Rubin, Y.N., and Dominic, D.F., 2004. Transport in heterogeneous sediments with multimodal conductivity and hierarchical organization across scales. Journal of Hydrology 294, 68-86, doi:10.1016/j.jhydrol.2003.10.024.

Dai, Z., Wolfsberg, A.V., Lu, Z., and Ritzi, R.W., 2007. Representing aquifer architecture in macrodispersivity models with an analytical solution of the transition probability matrix, Geophysical Research Letter 34, L20406, doi:10.1029/2007GL031608.

Deng, H., P.H. Stauffer, Z. Dai, Z. Jiao, R. Surdam, 2010a. Uncertainty in saline aquifer capacity and leakage: impacts of hydrological heterogeneity in the Rock Springs Uplift, Wyoming. GSA Abstracts with Programs, Vol. 42(5), 114, BTH 201. GSA 2010 Annual Meeting at Denver on 31 Oct. – 3 Nov.

Deng, H., P. H. Stauffer and H. S. Viswanathan, R. C. Surdam, and Z. Jiao, 2010b. Preliminary study on stress effects on $CO_2$ sequestration at Rock Springs Uplift, Wyoming. The Ninth Annual Conference on Carbon Capture & Sequestration, Pittsburg, PA.

Doughty, C. and Pruess, K., 2004. Modeling supercritical carbon dioxide injection in heterogeneous porous media. Vadose Zone Journal 3, 837-847.

Doughty, C., Freifeld, B.M., and Trautz, R.C., 2008. Site characterization for $CO_2$ geologic storage and vice versa: the Frio Brine Pilot, Texas, USA as a case study. Environmental Geology 54, 1635-1656.

Duan, Z., J. Hu, D. Li and S. Mao, 2008, Densities of the $CO_2$-$H_2O$ and $CO_2$-$H_2O$-NaCl systems up to 647 K and 100 MPa. Energy & Fuels 22, 1666-1674.

Duan, Z., R. Sun, C. Zhu and I.-M. Zhou, 2006, An improved model for the calculation of $CO_2$ solubility in aqueous solution containing $Na^+$, $K^+$, $Ca^{2+}$, $Mg^{2+}$, $Cl^-$, and $SO_4^{2-}$. Marine Chemistry 98, 131-139.

Ehlig-Economides, C. and Economides, M.J., 2010. Sequestering carbon dioxide in a closed underground volume. Journal of Petroleum Science and Engineering 70, 123-130.

Flett, M., Gurton, R., and Weir, G., 2007. Heterogeneous saline formations for carbon dioxide disposal: Impact of varying heterogeneity on containment and trapping. Journal of Petroleum Science & Engineering 57, 106-118.

Fox, J.E., Lambert, P.W., Mast, R.F., Nuss, N.W., and Rein, R.D., 1975. Porosity variation in the Tensleep and its equivalent, the Weber Sandstone, western Wyoming: A log and petrographic analysis. Rocky Mountain Association of Geology 12, 185-215.

Friedmann, S. J., 2003. Storing carbon in Earth. Geotimes, 2003 March.

Friedmann, S.J., 2007. Geological carbon dioxide sequestration. Elements 3, 179-184.

Gaus, I., 2010. Role and impact of $CO_2$-rock interactions during $CO_2$ storage in sedimentary rocks. International Journal of Greenhouse Gas Control 4, 73-89.

Gelhar, L.W., 1993. Stochastic Subsurface Hydrology, Prentice Hall, Englewood Cliffs, New Jersey.

Hein, J.R., R.B. Perkins, and B.R. McIntye, 2004. Evolution of thought concerning the origin of the phosphoria formation, western US phosphorate field. In: Life Cycle of the Phosphoria Formation: From Deposition toPost-Mining Environment, Edited by J.R. Hein. Elsevier, 19-42.

Ide, S.K., Jessen, K., and Orr Jr., F.M., 2010. Storage of $CO_2$ in saline aquifers: Effects of gravity, viscous, and capillary forces on amount and timing of trapping, International Journal of Greenhouse Gas Control 4, 481-491.

Journel, A.G., 1983. Nonparameteric estimation of spatial distributions. Mathematic Geology 15, 445-468, doi:10.1007/BF01031292.

Juanes, R., MacMinn, C.W., and Szulczewski, M.L., 2010. The footprint of the $CO_2$ plume during carbon dioxide storage in saline aquifers: storage efficiency for capillary trapping at the basin scale. Transport in Porous Media 82, 19-30.

Juanes, R., Spiteri, E.J., Orr Jr, F.M., and Blunt, M.J., 2006. Impact of relative permeability hysteresis on geological $CO_2$ storage, Water Resources Research 42, W12418 doi:10.1029/2005WR004806.

Kharaka, Y.K., Cole, D.R., Hovorka, S.D., Gunter, W.D., Knauss, K.G., and Freifeld, B.M., 2006. Gas-water-rock interactions in Frio formation following $CO_2$ injection: implications for the storage of greenhouse gases in sedimentary basins. Geology 34, 577-580.

Liu, B. and Y. Zhang, 2011. $CO_2$ modeling in a deep saline aquifer: a predictive uncertainty analysis using design of experiment. Environ. Sci. Technol., 45, doi:10.1021/es103187b.

Lucier, A., and Zoback, M.D., 2010. Assessing the economic feasibility of regional deep saline aquifer $CO_2$ injection and storage: a geomechanics-based workflow applied to the Rose Run sandstone in eastern Ohio, USA. International Journal of Greenhouse Gas Control 4, 230-247.

Lucier, A., Zoback, M.D., Gupta, N., and Ramakrishnan, T.S., 2006. Geomechanical aspects of $CO_2$ sequestration in a deep saline reservoir in the Ohio River Valley region. Environmental Geoscience 13, 85-103.

MacMinn, C.W., and Juanes, R., 2009. Post-injection spreading and trapping of $CO_2$ in saline aquifers: impact of the plume shape at the end of injection, Computer & Geoscience 13, 483-391 doi: 10.1007/s10596-009-9147-9.

MacMinn, C.W., and Juanes, R., 2010. $CO_2$ migration in saline aquifers. Part 1. Capillary trapping under slope and groundwater flow. J. Fluid Mech., 662, 329-351. doi:10.1017/S0022112010003319.

Michael, K., Golab, A., Shulakova, V., Ennis-King, J., Allinson, G., Sharma, S, and Aiken, T., 2010. Geological storage of $CO_2$ in saline aquifers – A review of the experience from existing storage operation. International Journal of Greenhouse Gas Control 4, doi:10.1016/j.ijggc.2009.12.011.

Matthews C.S. and C.S. Russel, 1967. Pressure buildup and flow rates in wells. Monograph of Society of Petroleum Engenderers, New York, Vol. 1, p10-17.

Miller, E. N., A.T. Meckel, and R.H. Trevino, 2010. Deciding on capacity calculation methodology for the Texas submerged lands capacity assessment. GSA Abstracts with Programs, Vol. 42(5), 114, BTH 202. GSA 2010 Annual Meeting at Denver on 31 Oct. – 3 Nov.

Montgomery, S.T., 1996. Brady Unit, Rock Springs Uplift, Wyoming: Migration and structural history. American Association of Petroleum Geology Bulletin 80, 1535-1546.

Nelson P.H. and J.E. Kibler, 2003. A Catalog of Porosity and Permeability from Core Plugs in Siliciclastic Rocks. USGS Open-file Report 03-420.

Neuzil, C.E., 1986. Groundwater flow in low-permeability environments. Water Resources Research 22, 1163-1195.

Neuzil, C.E., 1994. How permeable are clays and shales? Water Resources Research 30, 145-150.

Newmark, R.L., Friedmann, S.J., and S. A. Carroll, 2010. Water challenges for geologic carbon capture and sequestration. Environmental Management 45, 651-661.

Obi, E.-O.I. and Blunt, M.J., 2006. Streamline-based simulation of carbon dioxide storage in a North Sea aquifer, Water Resources Research 42, W03414 doi:10.1029/2004WR003347.

Person, M., Banerjee, A., Rupp, J., Medina, C., Lichtner, P., Gable, C., Pawar, R., Celia, M., McIntosh, J., and Bense, V., 2010. Assessment of basin-scale hydrologic impacts of $CO_2$ sequestration, Illinois basin. International Journal of Greenhouse Gas Control 4, doi:10.1016/j.ijggc.2010.04.004.

Piper, D.Z. and P.K. Link, 2002. An upwelling model for the Phophoria sea: A Permian, ocean-margin sea in the northwest United States. AAPG Bull. 86(7), 1217-1235.

Pruess, K., Garcia, J., Kovscek, T., Oldenburg, C., Rutqvist, J., Steefel, C., and Xu, T., 2004. Code intercomparison builds confidence in numerical methods for geological disposal of $CO_2$. Energy 29, 1431-1444.

Ritzi, W.R., Dai, Z., Dominic, D.F., and Rubin, Y.N., 2004. Spatial correlation of permeability in cross-stratified sediment with hierarchical architecture. Water Resources Research 40, W03513, doi:10.1029/2003WR002420.

Rutqvist, J., Birkholzer, J.T., and Tsang, C.F., 2008. Coupled reservoir-geomechanical analysis of the potential for tensile and shear failure associated with $CO_2$ injection in multilayered

reservoir-caprock systems, Intternational Journal of Rock Mechanics & Mining Science 45, 132-143.

Schnaar, G. and Digiulio, D.C., 2009. Computational modeling of the geologic sequestration of carbon Dioxide. Vadose Zone Journal 8, 389-403.

Shiraki, R., Dunn, T.L., 2000. Experimental study on water-rock interactions during $CO_2$ flooding in the Tensleep formation, Wyoming, USA. Applied Geochemistry 15, 265-279.

Silva, AJ, JR Hetherman, and DI Calnan, 1981, Low-gradient permeability testing of fine-grained marine sediments. In: Zimmie, TF and CO Riggs ed., Permeability and groundwater contaminant transport. American Society for Testing and Materials Special Technical Publication 764, 121-136.

Span, R., and W. Wagner, 1996. A new equationof state for carbon dioxide covering the fluid region from the triple-point temperature to 1100 K at pressure up to 800 MPa. J. Phys. Chem. Ref. Data, 25(6), 1509-1596.

Stauffer, P.H., R.C. Surdam, Z. Jiao, T.A. Miller, and R.D. Bentley, 2009a. Combining geologic data and numerical modeling to improve estimates of the $CO_2$ sequestration potential of the Rock Springs Uplift, Wyoming. Energy Procedia 1, GHGT-9, 2717-2724.

Stauffer, P.H., R.J. Pawar, R.C. Surdam, Z. Jiao, H. Deng, B.C. Lettelier, H.S. Viswanathan, D. L. Sanzo and G. N. Keating, 2010. Application of CO2-PENS risk analysis tool to the Rock Springs Uplift, Wyoming. Energy Procedia 2, GHGT-10 (in press).

Stauffer, P.H., H.S. Viswanathan, R.J. Pawar and G.D. Guthrie, 2009b. A system model for geologic sequestration of carbon dioxide. Environmental Science & Technology 43, 565-570.

Surdam, R.C., Jiao, Z., Stauffer, P.H., and Miller, T., 2009. An integrated strategy for carbon management combing geological $CO_2$ sequestration, displaced fluid production, and water treatment. Wyoming State Geological Survey, Challenges in Geologic Resource Development No.8.

Surdam, R.C.. and Jiao, Z., 2007. The Rock Springs Uplift: An outstanding geological $CO_2$ sequestration site in southwest Wyoming. Wyoming State Geological Survey, Challenges in Geologic Resource Development No.2.

Tompson, A.F.B., 1993. Numerical simulation of chemical migration in physically and chemically heterogeneous porous media. Water Resources Research 29, 3709-3726 doi:10.1029/93WR01526.

Tsang, C.-F., Birkholzer, J., and Rutqvist, J., 2008. A comparative review of hydrologic issues involved in geologic storage of $CO_2$ and injection disposal of liquid waste. Environmental Geology 54, 1723-1737.

Turcotte, D.L. and G. Schubert, 2002, Geodynamics, 2nd edition, p393-401.

USDOE (U. S. Department of Energy), 2007. Methodology for development of Carbon sequestration capacity estimates. Appendix a in: Carbon Sequestration Atlas of United States and Canada, National Energy Technology Laboratory, Pittsburgh, PA, USA.

Vilarrasa, V., D. Bolster, M. Dentz, S. Olivella and J. Carrera, 2010. Effects of CO2 Compressibility on CO2 storage in Deep saline aquifers. Transp Porous Med., 85(3), 619-639.

Viswanathan, H.S., Pawar, R.J., Stauffer, P.H., Kaszuba, J.P., Carey, J.W., Olsen, S.C., Keating, G.N., Kavetski, D., and Guthrie, G.D., 2008. Development of a hybrid process and system model for the assessment of wellbore leakage at a geologic $CO_2$ sequestration site. Environmental Science & Technology 42, 7280-7286.

Wilkin, R.T. and Digiulio, D.C., 2010. Geochemical impactions to groundwater from geologic carbon sequestration: controls on pH and inorganic carbon concentrations from reaction path and kinetic modeling. Environmental Science & Technology 44, 4821-4827.

Wilson, E.J., Friedmann, S.J., and Pollak, M.F., 2003. Research for Deployment: Incorporating risk, regulation, and liability for carbon capture and sequestration. Environmental Science & Technology 41, 5945-5952.

Xu, T., Apps, J.A. and Pruess, K., 2004. Numerical simulation of $CO_2$ disposal by mineral trapping in deep aquifers. Appllied Geochemistry 19, 917-936.

Yang, Y. and Aplin A.C., 2010. A permeability-porosity relationship for mudstone. Marine and Petroleum Geology 27, 1692-1697.

Ye, M. and Khaleel, R., 2008. A Markov chain model for characterizing medium heterogeneity and sediment layering structure. Water Resources Research 44, W09427, doi:10.1029/2008 WR006924.

Zhou, Q., Birkholzer, J.T., Tsang, C.F., and Rutqvist, J., 2008. A method for quick assessment of $CO_2$ storage capacity in closed and semi-closed saline formations. International Journal of Greenhouse Gas Control 2, 626-639.

Zhou, Q., J.T. Birkholzer and C.-F. Tsang, 2009. A semi-Analytical solution for large-scale injection-induced pressure perturbation and leakage in a laterally bounded aquifer-aquitard system. Transp Porous Med., 78(1), 127-148.

Zyvoloski, G.A., Robinson, B.A., Dash, Z.V., and Trease, L.L., 1997. Summary of the models and methods for the FEHM application - A finite element heat-and mass-transfer code. Rep. LA-13307-MS, Los Alamos National Laboratory, Los Alamos, New Mexico.

Tables

Table 1. Density porosity classification for each formation and corresponding mean permeability

| Formations | Category | Density porosity $n$ (%) | Volume portion (%) | Mean porosity $\phi$ (%) | Standard deviation $\phi$ (%) | Permeability $k$ (mD) |
|---|---|---|---|---|---|---|
| Chugwater Formation | 1 - low | $n \leq 5$ | 0.591 | 2.58 | 1.52 | 0.0000056 |
| | 2 - mediate | $5 < n \leq 15$ | 0.358 | 8.88 | 3.19 | 0.00018 |
| | 3 - high | $n > 15$ | 0.051 | 24.01 | 4.68 | 0.022 |
| Phosphoria Formation | 1 - low | $n \leq 5$ | 0.75 | 2.58 | 1.52 | 0.014 |
| | 2 - high | $n > 5$ | 0.25 | 10.15 | 7.53 | 1.277 |
| Weber Sandstone | 1 - low | $n \leq 5$ | 0.699 | 2.63 | 1.52 | 0.165 |
| | 2 - mediate | $5 < n \leq 15$ | 0.286 | 8.87 | 3.20 | 2.673 |
| | 3 - high | $n > 15$ | 0.015 | 24.88 | 4.99 | 3374 |
| Madison Limestone | 1 - low | $n \leq 5$ | 0.62 | 2.69 | 1.67 | 0.001 |
| | 2 - mediate | $5 < n \leq 15$ | 0.267 | 8.55 | 3.34 | 0.847 |
| | 3 - high | $n > 15$ | 0.113 | 19.20 | 3.43 | 10.269 |

Note: using empirical power law between porosity and permeability (Bernabe et al., 2003), $k = a\phi^b$ , estimates permeability based on $a = 1.5\times10^{-12}$ m$^2$ and $b = 3.0$ for Madison and Phosphoria. Using $\log k = 0.1937\phi - 1.2911$ for Weber sandstone (Fig. 3). For cap rock, Chugwater formation, an equation from Yang & Aplin (2010) is used to calculate permeability, that is $\ln k = -69.59 - 26.79 \cdot C + 44.07 \cdot C^{0.5} + (-53.61 - 80.03 \cdot C + 132.78 \cdot C^{0.5}) \cdot e + (86.61 + 81.91 \cdot C - 163.61 \cdot C^{0.5}) \cdot e^{0.5}$, where void ratio $e = \phi / (1- \phi)$ (Fig. 4), and $C$ is the clay percentage in cap-rocks.

Table 2. Global means and global variance for porosity and permeability for geological formations

| Formations | Porosity $\phi$ (%) | | Permeability log k ($m^2$) | |
|---|---|---|---|---|
| | Global Mean | Global Variance | Global Geometric Mean | Global Variance |
| Chugwater | 5.93 | 28.70 | -18.23 | 1.38 |
| Phosphoria | 4.47 | 13.77 | -17.31 | 3.54 |
| Weber | 4.75 | 16.13 | -14.90 | 0.69 |
| Madison | 6.12 | 30.52 | -14.45 | 2.35 |

Table 3. Simulation results of ten runs with different combinations of permeability realizations for 50 years of $CO_2$ injection

| Simulating runs | $TCO_2$ (Mt) | $TH_2O$ (Mt) | $TCO_2/TH_2O$ |
|---|---|---|---|
| Perm_6606_p75 | 496.085 | 416.539 | 1.19 |
| Perm_6646_p75 | 662.465 | 598.729 | 1.11 |
| Perm_6686_p75 | 584.149 | 506.559 | 1.15 |
| Perm_6666_p75 | 484.796 | 407.371 | 1.19 |
| Perm_4404_p75 | 530.550 | 440.041 | 1.21 |
| Perm_4464_p75 | 518.158 | 432.422 | 1.20 |
| Perm_0000_p75 | 483.191 | 404.102 | 1.20 |
| Perm_0060_p75 | 477.616 | 404.532 | 1.18 |
| Perm_6040_p75 | 650.283 | 591.476 | 1.10 |
| Perm_6080_p75 | 567.347 | 493.181 | 1.15 |
| Perm_1111_p75 | 525.660 | 429.102 | 1.23 |
| Perm_2222_p75 | 467.828 | 370.878 | 1.26 |
| Perm_3333_p75 | 583.564 | 510.981 | 1.14 |
| Perm_4444_p75 | 671.757 | 594.036 | 1.13 |
| Perm_5555_p75 | 569.270 | 489.805 | 1.16 |
| Perm_7777_p75 | 607.864 | 547.467 | 1.11 |
| Perm_8888_p75 | 496.927 | 410.596 | 1.21 |
| Perm_9999_p75 | 478.933 | 380.223 | 1.26 |
| perm_4414_p75 | 561.500 | 462.806 | 1.21 |
| Perm_4424_p75 | 596.936 | 497.699 | 1.20 |
| Perm_4434_p75 | 678.264 | 606.441 | 1.12 |
| Perm_4454_p75 | 602.875 | 511.143 | 1.18 |
| Perm_4474_p75 | 667.322 | 596.143 | 1.12 |
| Perm_4494_p75 | 592.823 | 491.001 | 1.21 |
| perm_6696_p75 | 595.745 | 503.617 | 1.18 |
| Perm_9909_p75 | 431.580 | 346.385 | 1.25 |
| Perm_9949_p75 | 604.599 | 536.523 | 1.13 |
| Perm_6555_p75 | 616.781 | 536.223 | 1.15 |
| Perm_6999_p75 | 514.716 | 427.813 | 1.20 |
| Perm_6444_p75 | 692.904 | 631.939 | 1.10 |
| Perm_6616_p75 | 525.548 | 439.487 | 1.20 |
| Perm_6626_p75 | 552.747 | 459.763 | 1.20 |
| Perm_6636_p75 | 657.472 | 591.989 | 1.11 |
| Perm_6656_p75 | 523.835 | 447.158 | 1.17 |
| Perm_6676_p75 | 635.027 | 572.396 | 1.11 |
| Perm_9939_p75 | 584.424 | 515.404 | 1.13 |
| Perm_9969_p75 | 425.842 | 343.847 | 1.24 |
| Perm_9929_p75 | 495.828 | 397.325 | 1.25 |
| Perm_9959_p75 | 505.183 | 417.423 | 1.21 |
| Perm_9979_p75 | 583.820 | 516.930 | 1.13 |
| Perm_9989_p75 | 507.098 | 425.200 | 1.19 |
| Perm_9919_p75 | 454.244 | 359.615 | 1.26 |
| Average | 558.656 | 477.674 | 1.18 |
| Stand deviation | 71.624 | 78.870 | 0.05 |
| Variation Coefficient | 12.82% | 16.51% | 4.11% |
| Minimum | 692.904 | 631.939 | 1.263 |
| Median | 564.424 | 476.306 | 1.186 |
| Maximum | 425.842 | 343.847 | 1.096 |

Note: $TCO_2$ = Total CO2 injected, $TH_2O$ = Total water produced

Table 4. Calculation of $CO_2$ storage capacity at RSU, Wyoming

| Category items | New Estimation in this study | | Estimation in Surdam et al (2007) |
|---|---|---|---|
| | Simulation domain | RSU | RSU |
| Average/effective porosity for the Weber Sandstone (%) | 4.75 | 4.75 | 10.0 |
| Saline aquifer property | Heterogeneous | Heterogeneous | Homogenous |
| Area ($km^2$) | 256 | 3328 | 3328 |
| Saline aquifer volume ($m^3$) | $5.81\times10^{10}$ | $6.88\times10^{11}$ | $6.88\times10^{11}$ |
| $CO_2$ mass stored (Mt) | $558.7 \pm 21.7$ | $6614 \pm 256$ | 18400 |
| Brine mass produced (Mt) | $477.7 \pm 23.9$ | $5855 \pm 282$ | |
| Average $CO_2$ release (Mt/year) | | 54.4 | 54.4 |
| Injection duration (year) | 50 | 122 | 338 |

Note: the ranges of storage capacity and produced brine are given at 95% confidence interval.

Table 5. Leakage of $CO_2$ into cap-rocks at the end of 50 years of $CO_2$ injection

| Simulation runs | Phosphoria (Mt) | Chugwater (Mt) | Nugget (Mt) | Total $CO_2$ Leaked (Mt) | Leakage1 (%) | Leakage2 (%) |
|---|---|---|---|---|---|---|
| Perm_6606_p75 | 49.660 | 2.351 | 0.000 | 52.011 | 10 | 0.47 |
| Perm_6646_p75 | 85.131 | 3.259 | 0.000 | 88.390 | 13 | 0.49 |
| Perm_6686_p75 | 84.310 | 2.871 | 0.000 | 87.181 | 15 | 0.49 |
| Perm_6666_p75 | 85.273 | 2.773 | 0.000 | 88.046 | 18 | 0.57 |
| Perm_4404_p75 | 52.967 | 1.119 | 0.000 | 54.086 | 10 | 0.21 |
| Perm_4464_p75 | 86.313 | 1.415 | 0.000 | 87.728 | 17 | 0.27 |
| Perm_0000_p75 | 53.032 | 0.910 | 0.000 | 53.942 | 11 | 0.19 |
| Perm_0060_p75 | 68.377 | 0.896 | 0.000 | 69.273 | 15 | 0.19 |
| Perm_6040_p75 | 103.535 | 3.731 | 0.000 | 107.266 | 16 | 0.57 |
| Perm_6080_p75 | 89.016 | 2.992 | 0.000 | 92.008 | 16 | 0.53 |
| Perm_1111_p75 | 102.590 | 0.839 | 0.000 | 103.429 | 20 | 0.16 |
| Perm_2222_p75 | 50.199 | 0.46 | 0.000 | 50.659 | 11 | 0.10 |
| Perm_3333_p75 | 35.493 | 0.038 | 0.000 | 35.531 | 6 | 0.01 |
| Perm_4444_p75 | 97.888 | 1.338 | 0.000 | 99.226 | 15 | 0.20 |
| Perm_5555_p75 | 12.181 | 0.018 | 0.000 | 12.199 | 2 | 0.00 |
| Perm_7777_p75 | 65.581 | 0.151 | 0.000 | 65.732 | 11 | 0.02 |
| Perm_8888_p75 | 84.752 | 0.338 | 0.000 | 85.090 | 17 | 0.07 |
| Perm_9999_p75 | 43.981 | 0.229 | 0.000 | 44.210 | 9 | 0.05 |
| perm_4414_p75 | 83.013 | 1.152 | 0.000 | 84.165 | 15 | 0.21 |
| Perm_4424_p75 | 88.146 | 1.740 | 0.000 | 89.886 | 15 | 0.29 |
| Perm_4434_p75 | 52.437 | 0.767 | 0.000 | 53.204 | 8 | 0.11 |
| Perm_4454_p75 | 43.685 | 1.016 | 0.000 | 44.701 | 7 | 0.17 |
| Perm_4474_p75 | 115.018 | 2.162 | 0.000 | 117.180 | 18 | 0.32 |
| Perm_4494_p75 | 52.437 | 0.767 | 0.000 | 53.204 | 9 | 0.13 |
| perm_6696_p75 | 73.008 | 2.336 | 0.000 | 75.344 | 13 | 0.39 |
| Perm_9909_p75 | 24.994 | 0.349 | 0.000 | 25.343 | 6 | 0.08 |
| Perm_9949_p75 | 45.125 | 0.409 | 0.000 | 45.534 | 8 | 0.07 |
| Perm_6555_p75 | 30.156 | 0.155 | 0.000 | 30.311 | 5 | 0.03 |
| Perm_6999_p75 | 42.152 | 0.209 | 0.000 | 42.361 | 8 | 0.04 |
| Perm_6444_p75 | 104.892 | 2.272 | 0.000 | 107.164 | 15 | 0.33 |
| Perm_6616_p75 | 103.582 | 2.879 | 0.000 | 106.461 | 20 | 0.55 |
| Perm_6626_p75 | 100.241 | 2.859 | 0.000 | 103.100 | 19 | 0.52 |
| Perm_6636_p75 | 76.882 | 2.385 | 0.000 | 79.267 | 12 | 0.36 |
| Perm_6656_p75 | 53.337 | 1.672 | 0.000 | 55.009 | 11 | 0.32 |
| Perm_6676_p75 | 84.817 | 2.939 | 0.000 | 87.756 | 14 | 0.46 |
| Perm_9939_p75 | 41.800 | 0.361 | 0.000 | 42.161 | 7 | 0.06 |
| Perm_9969_p75 | 55.845 | 0.513 | 0.000 | 56.358 | 13 | 0.12 |
| Perm_9929_p75 | 47.504 | 0.414 | 0.000 | 47.918 | 10 | 0.08 |
| Perm_9959_p75 | 27.028 | 0.227 | 0.000 | 27.255 | 5 | 0.04 |
| Perm_9979_p75 | 71.755 | 0.714 | 0.000 | 72.469 | 12 | 0.12 |
| Perm_9989_p75 | 69.744 | 0.365 | 0.000 | 70.109 | 14 | 0.07 |
| Perm_9919_p75 | 62.804 | 0.419 | 0.000 | 63.223 | 14 | 0.09 |
| Average | 66.683 | 1.305 | 0 | 67.988 | 12 | 0.23 |
| Standard deviation | 25.514 | 1.087 | 0 | 26.293 | 4 | 0.18 |
| Variation Coefficient | 38% | 83% | - | 39% | 36% | 78% |

Note: The amount of $CO_2$ leaking into cap-rocks is calculated by summation of dissolved and supercritical $CO_2$. Leakage1 (%) = (Total $CO_2$ leaked / Total $CO_2$ injected) × 100. Leakage2 (%) = ($CO_2$ leaked into Chugwater / Total $CO_2$ injected) × 100.

Table 6. Parameters used for discussion in this study

| Parameters | Symbol | Unit | Values |
|---|---|---|---|
| Saline aquifer effective permeability | $k$ | $m^2$ | $1\times10^{-15}$ |
| Saline aquifer effective Porosity | $\phi$ | % | 5 |
| Saline aquifer thickness | $b$ | m | 200 |
| Saline aquifer salinity | $s$ | % | 2 |
| Saline aquifer thermal onductivity | $\lambda_m$ | W/K m | 3.3 |
| Saline aquifer initial fluid pressure | $P_{inf}$ | MPa | |
| Maximum Temperature difference | $\Delta T$ | °C | 15 |
| Brine viscosity | $\mu_w$ | Pa s | $1.33\times10^{-4}$ |
| Brine density | $\rho_w$ | $kg/m^3$ | 1100 |
| $CO_2$ fluid viscosity | $\mu_c$ | Pa s | $5.8\times10^{-5}$ |
| $CO_2$ fluid density | $\rho_c$ | $kg/m^3$ | 860 |
| Brine compressibility | $c_w$ | $Pa^{-1}$ | $3.5\times10^{-10}$ |
| $CO_2$ fluid compressibility | $c_c$ | $Pa^{-1}$ | $1.0\times10^{-9}$ |
| Pore compressibility | $c_p$ | $Pa^{-1}$ | $4.5\times10^{-10}$ |
| Injection time | $t$ | year | 50 |
| Specific storage | $Ss$ | - | $5\times10^{-6}$ |
| Injection rate | $Q$ | kg/s | |
| Gravitational acceleration | $g$ | $m/s^2$ | 9.8 |
| Residual water saturation | $\theta_{wr}$ | % | 10 |
| Maximum water saturation | $\theta_{ws}$ | % | 90 |
| Residual $CO_2$ saturation | $\theta_{CO2r}$ | % | 10 |
| Maximum $CO_2$ saturation | $\theta_{CO2s}$ | % | 90 |
| Brine thermal expansion | $\alpha_f$ | $K^{-1}$ | 0.001 |
| Brine specific heat capacity | $c_{pf}$ | J/kg K | $4.2\times10^3$ |

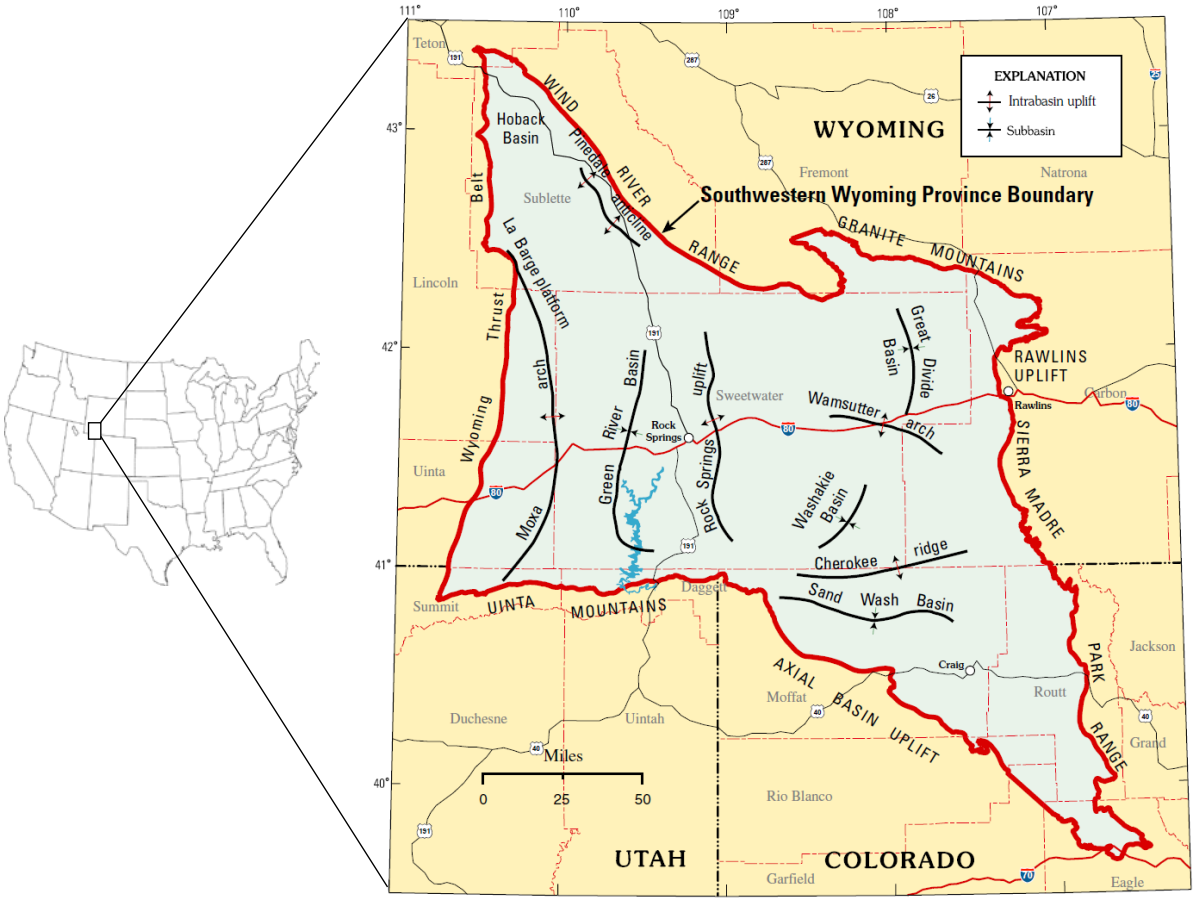


Fig.1. Geological structures within the Southwestern Wyoming Province. Map in the right from Finn and Johnson (2005).

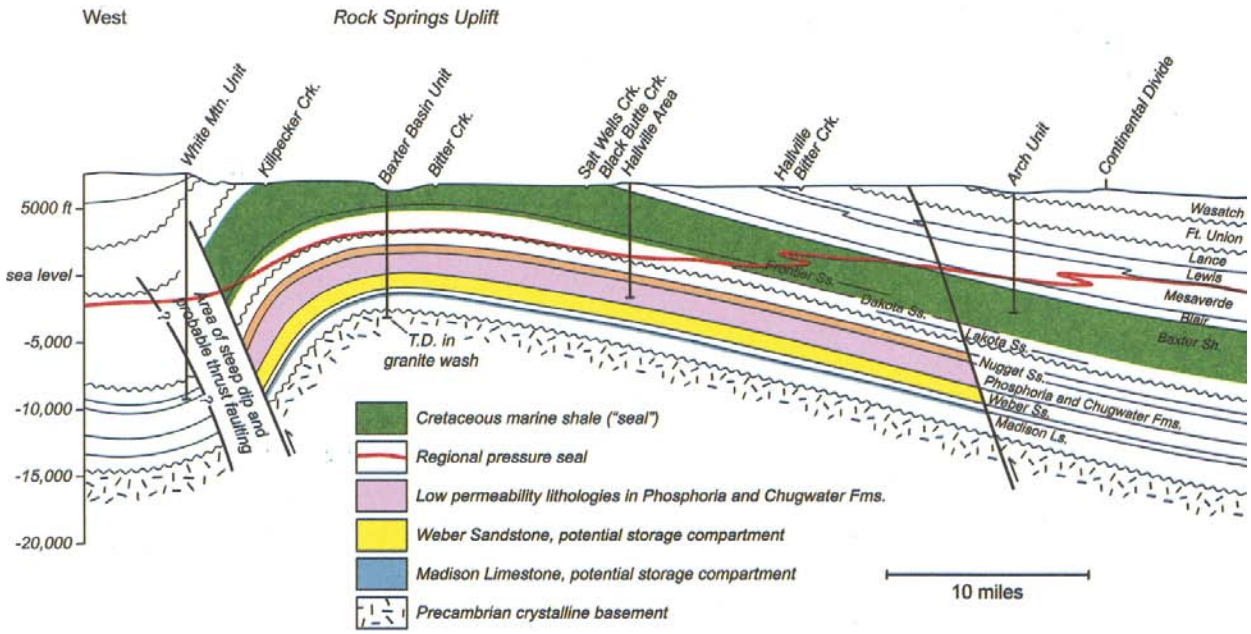


Fig.2. East-west cross-section of Rock Springs Uplift (From Surdam et al., 2007).

| Era | System | Epoch | Formations |
|---|---|---|---|
| **Cenozoic** | Miocene | | Wasatch |
| | Paleocene | | Fort Union |
| **Mesozoic** | Cretaceous | Late | Lance |
| | | | Fox Hill |
| | | | Lewis Shale |
| | | | Almond |
| | | | Ericson Sandstone |
| | | | Rock Springs |
| | | | Blair |
| | | | Baxter Shale |
| | | | Frontier |
| | | | Mowry Shale |
| | | Early | Dakota |
| | Jurassic | Late | Morrison |
| | | Middle | Entrada |
| | | Early | Nugget Sandstone |
| | Triassic | Late | |
| | | | Chugwater |
| **Paleozoic** | Permian | | Phosphoria |
| | Pennsylvanian | | Weber Sandstone |
| | | | Amsden |
| | Mississippian | | Madison Limestone |
| **Precambrian** | Metamorphic Bedrocks | | |

Fig.3. Sketch of stratigraphic column of Rock Springs Uplift.

Figures

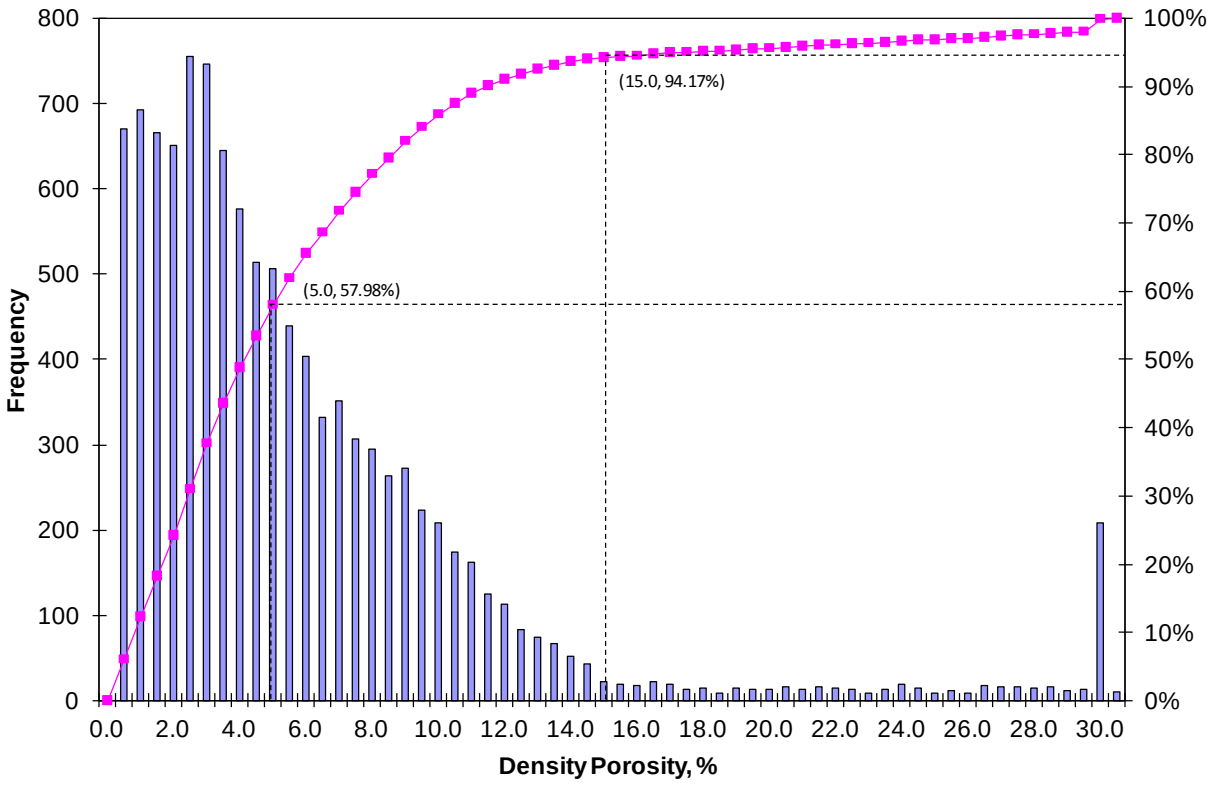


Fig.4. Density well log based porosity histogram of Weber sandstone from 15 well logs, Rock Springs Uplift.

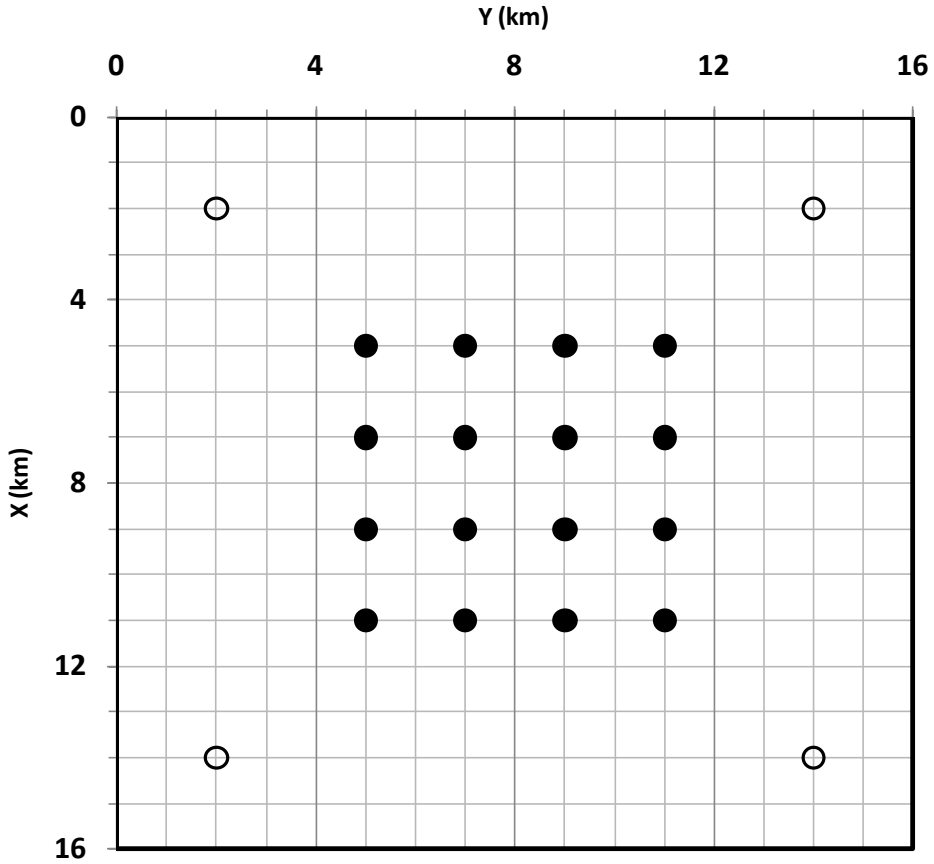


Fig. 5. Horizontal plane view of simulation domain size and locations for sixteen injection wells (black solid circles) and four pumping wells (open circles).

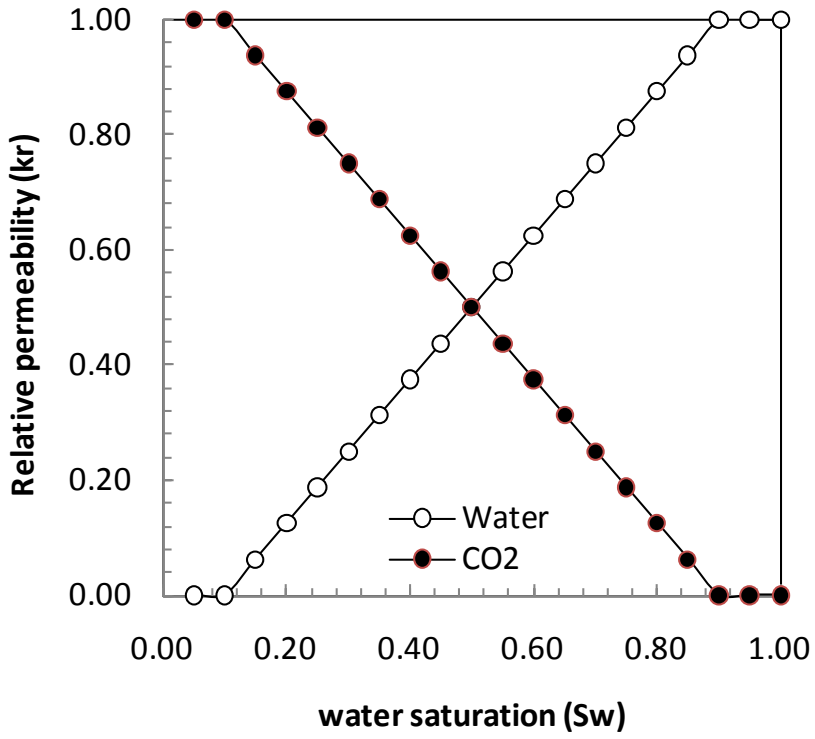


Fig.6. Linear relative permeability model used to simulate $CO_2$-brine multiphase flow

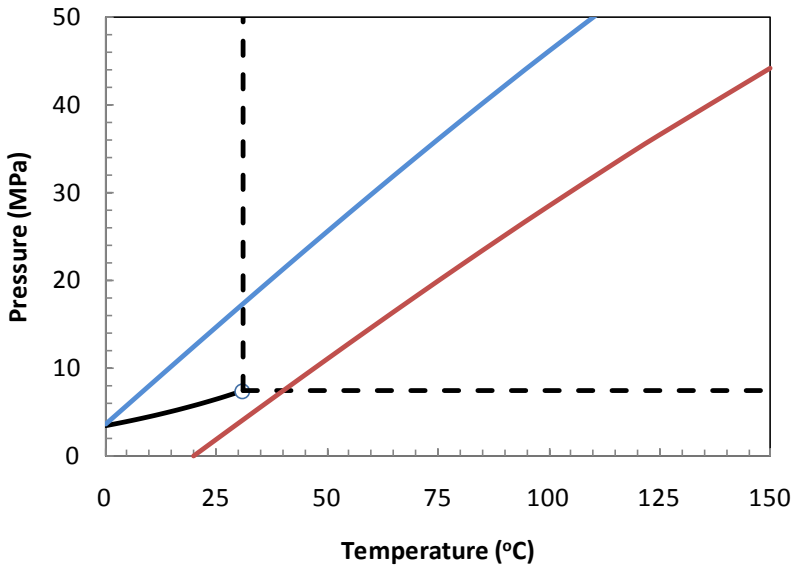


Fig.7. Pressure and temperature regime between the blue and the red lines is potential range for Rock Springs Uplift. The blue line indicates a relatively cold geothermal gradient of 22 °C/km with a mean winter temperature of -8°C on surface; the red line denotes a relatively hot geothermal gradient of 26.4 °C/km with a mean summer temperature 20°C on surface. The black solid line is the pure $CO_2$ saturation line (calculated from equation of Span & Wagner, 1996) and the open circle stands for the critical point of $CO_2$ (30.978°C, 7.377MPa).

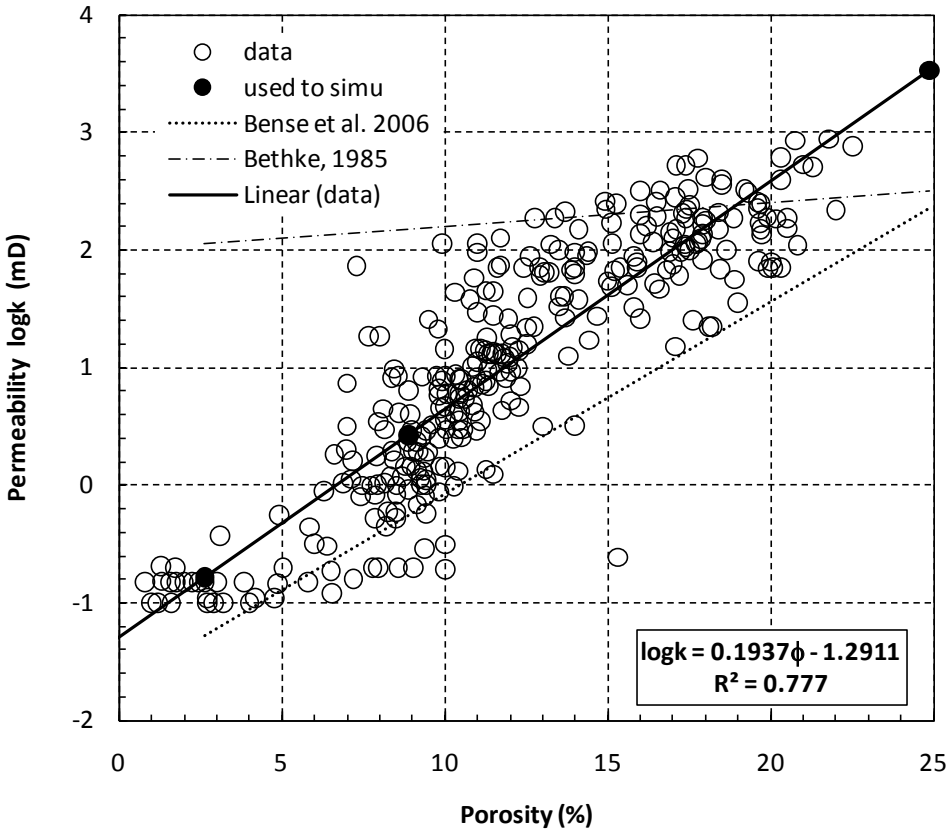


Fig.8. Porosity-permeability relationship for Weber sandstone in basins in Wyoming. Solid circles stand for parameter values used in numerical simulation in this study.

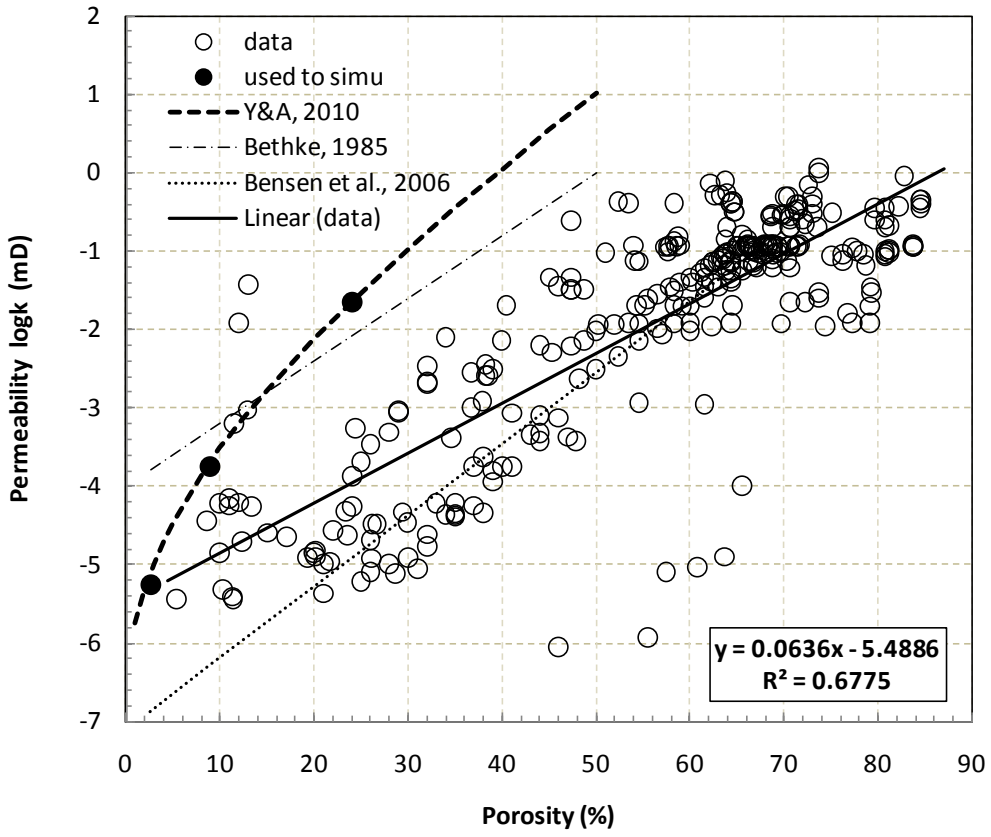


Fig.9. Porosity-permeability relationship in mudstones and shales worldwide. Solid circles stand for parameter values used for cap rock (Chugwater formation) in numerical simulation in this study.

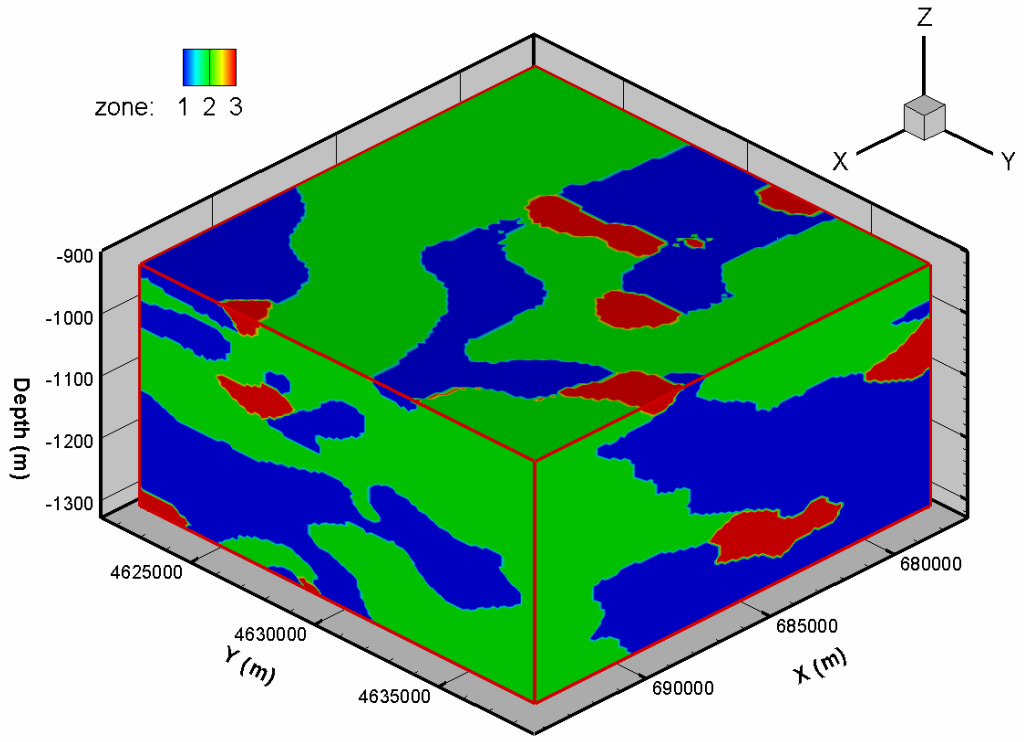


(a)

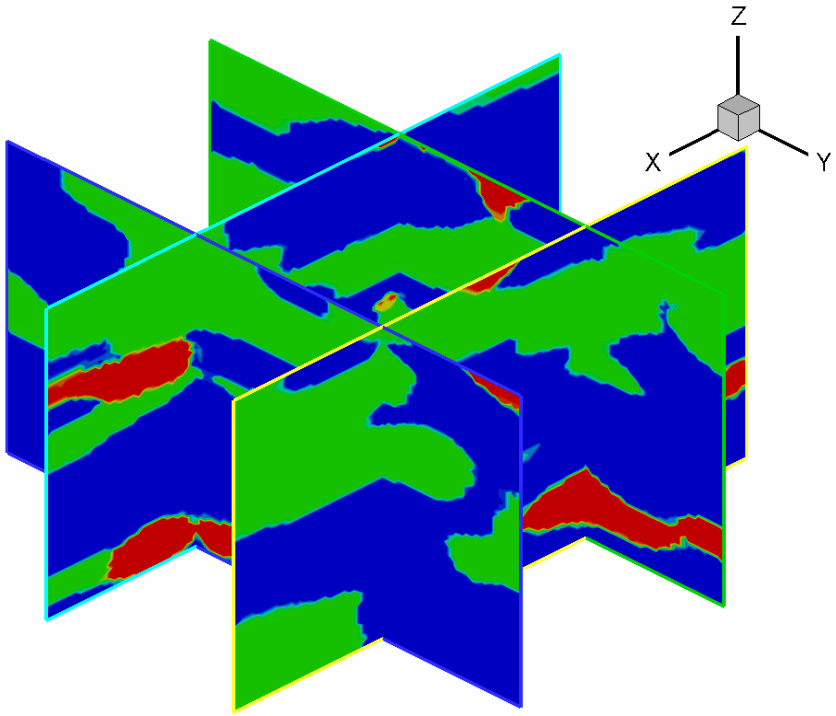


(b)

Fig. 10. Random indicator field of realization 1 generated for for Chugwater Formation

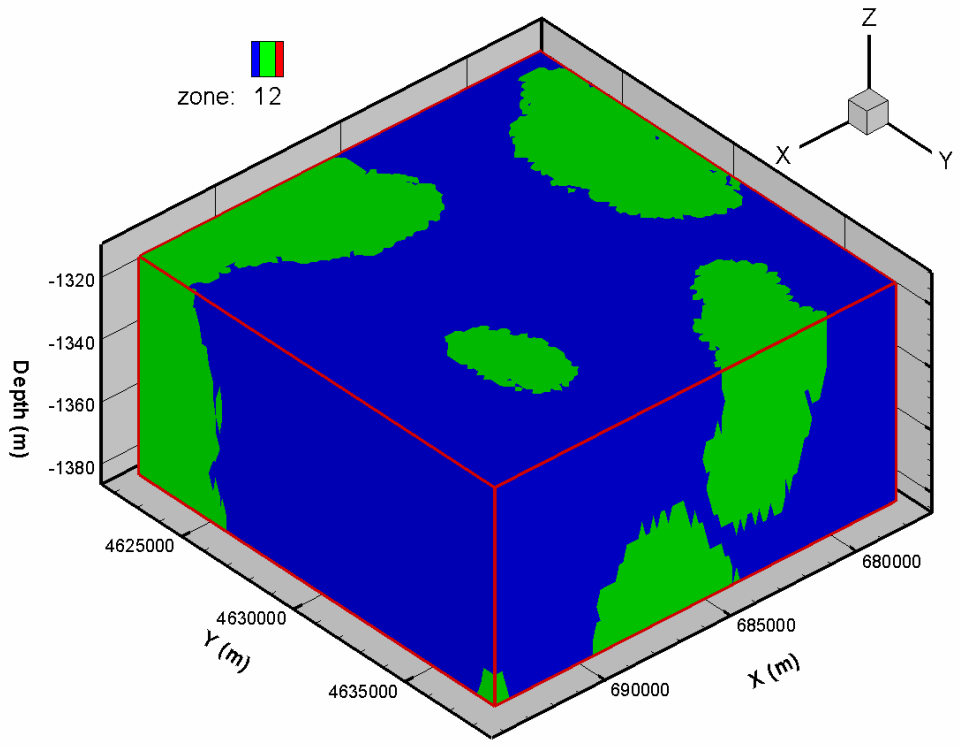


(a)

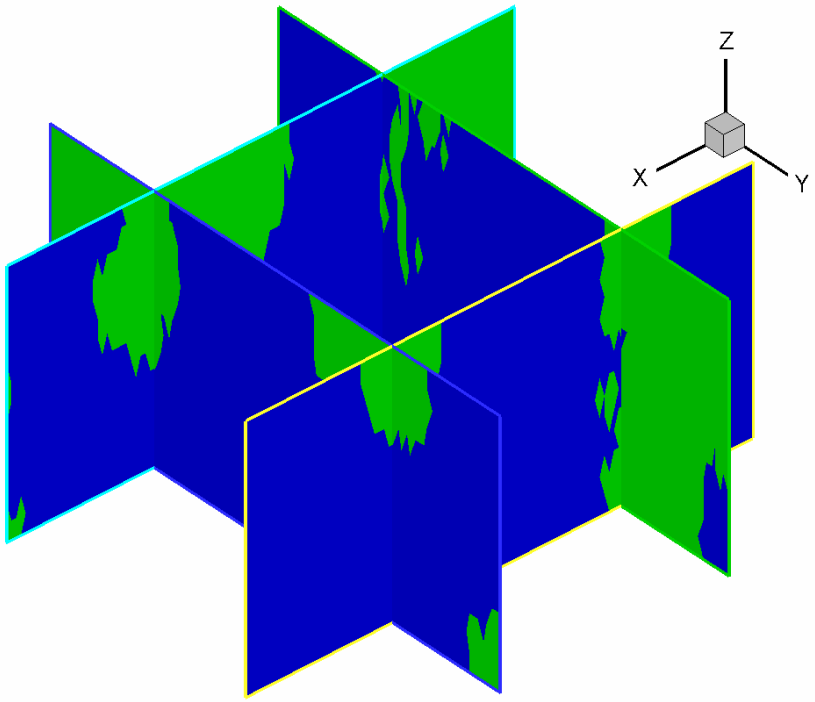


(b)

Fig. 11. Random indicator field of realization 1 generated for Phosphoria Formation

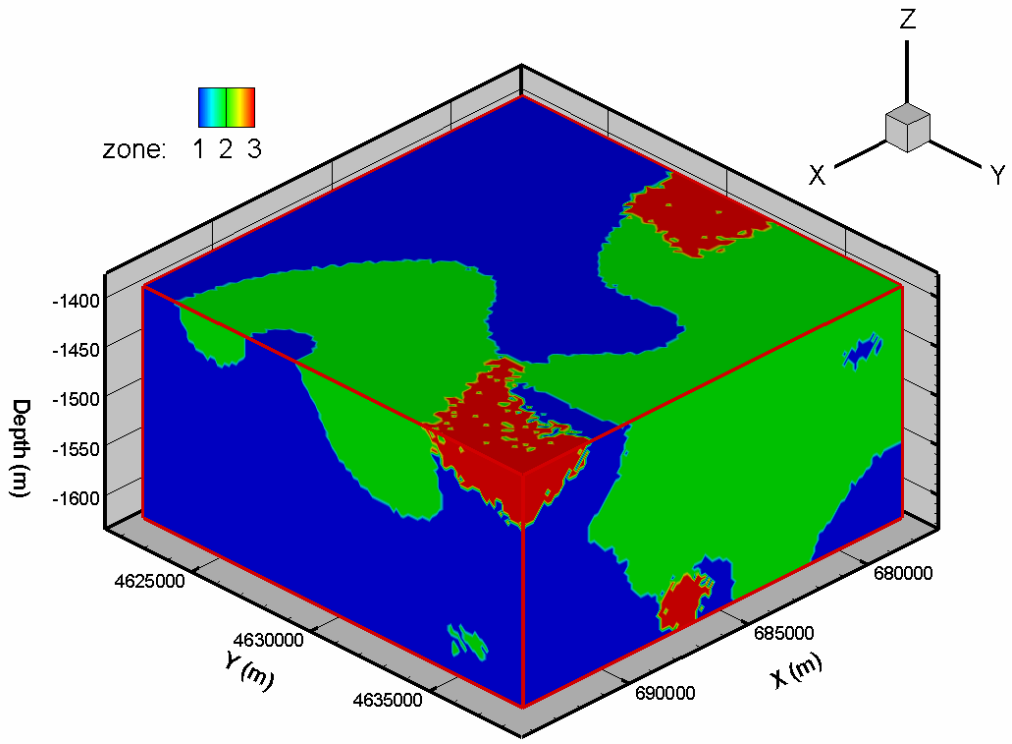


(a)

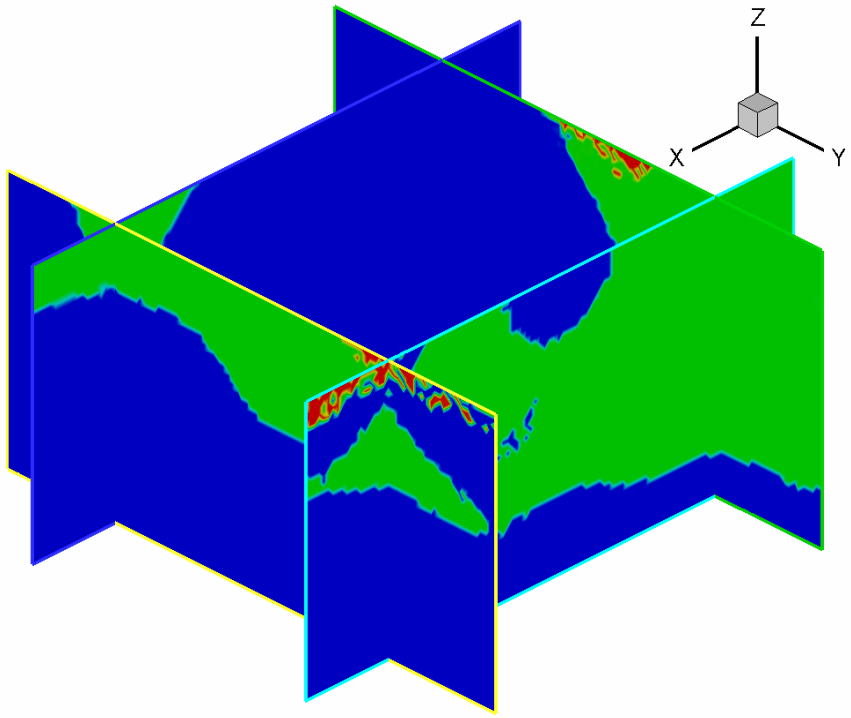


(b)

Fig. 12. Random indicator field of realization 1 generated for Weber Formation sandstone

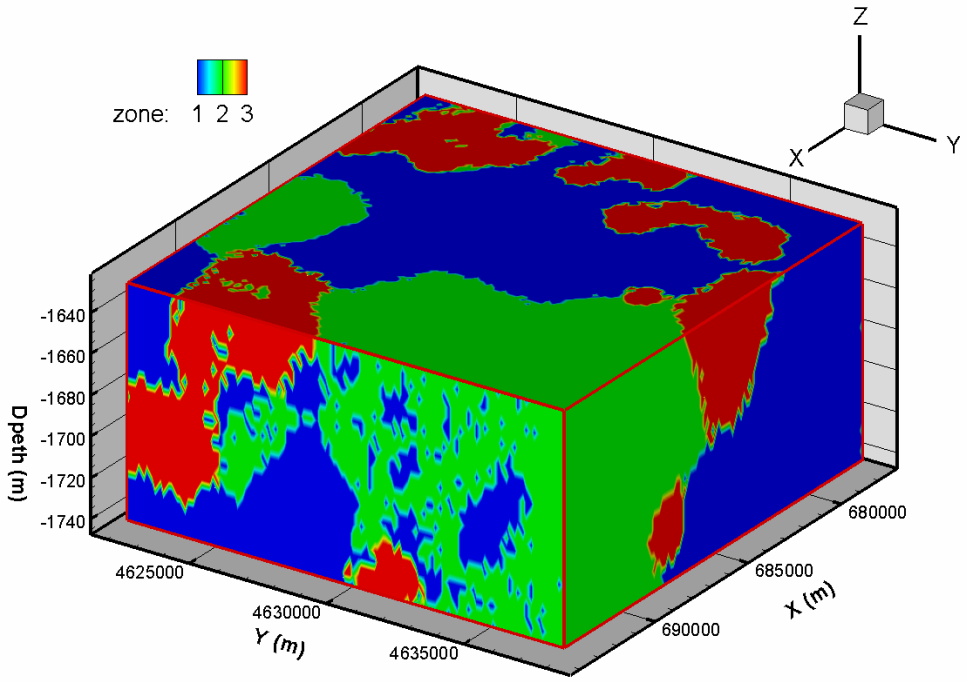


(a)

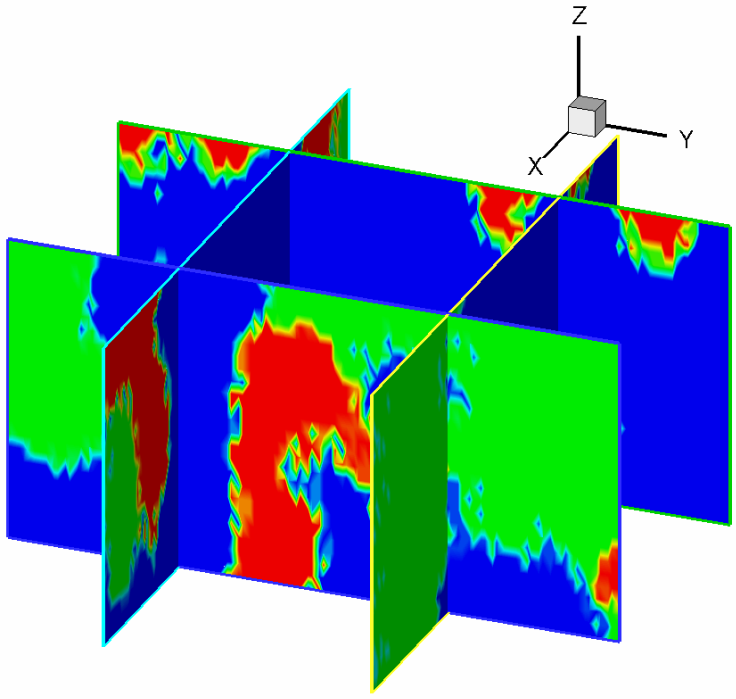


(b)

Fig. 13. Random indicator field of realization 1 generated for Madison Formation limestone

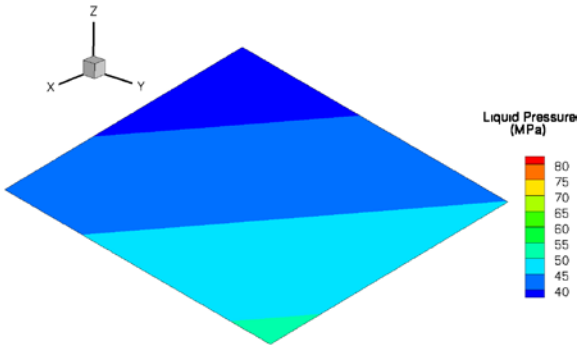


(a) Before injection of $CO_2$

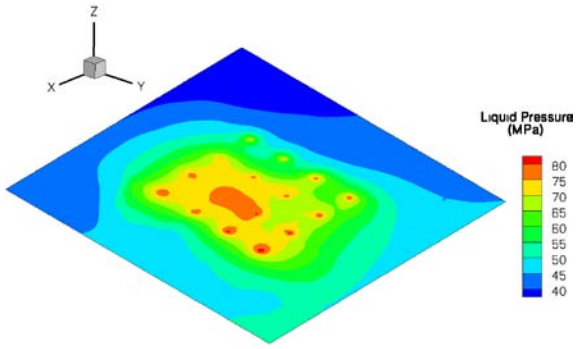


(b) Injecting $CO_2$ for 1 year

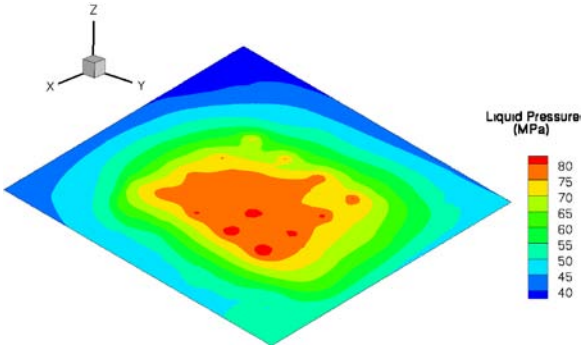


(c) Injecting $CO_2$ for 10 years

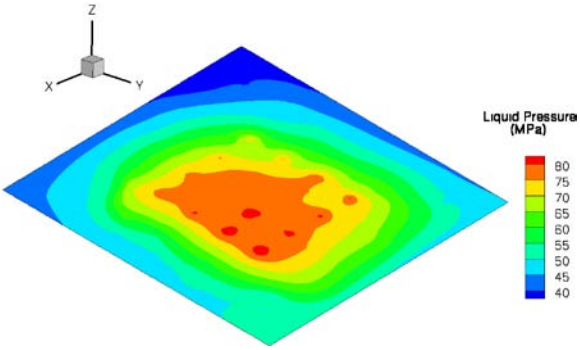


(d) Injecting $CO_2$ for 20 years

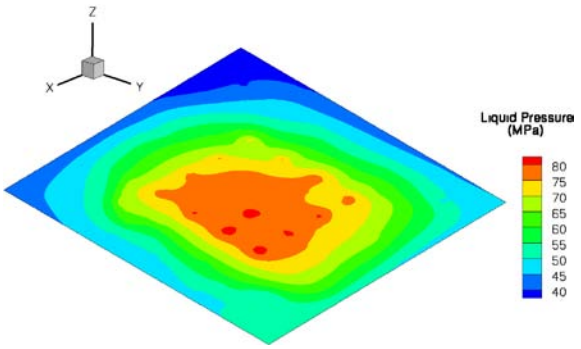


(e) Injecting $CO_2$ for 40 years

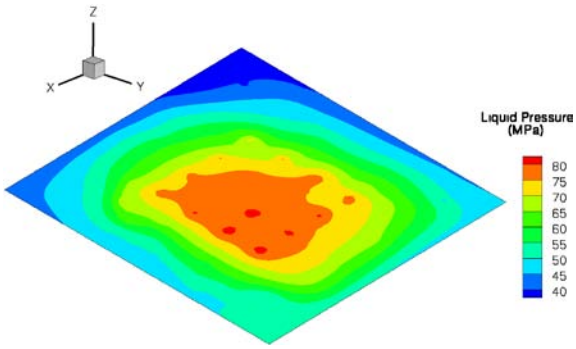


(f) Injecting $CO_2$ for 50 years

Fig. 14. Contours of the liquid pressure show pressure building up along the bottom of the Weber sandstone, where 16 injection wells locate in the center.

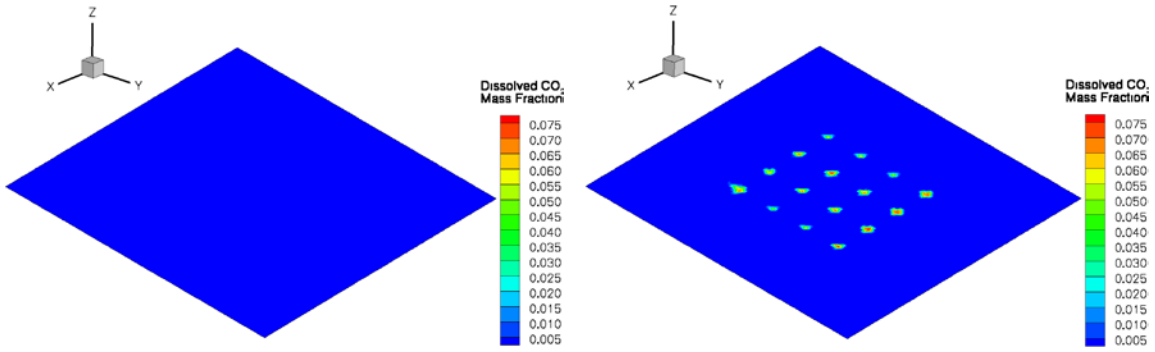


(a) Before injection of $CO_2$ (b) Injecting $CO_2$ for 1 year

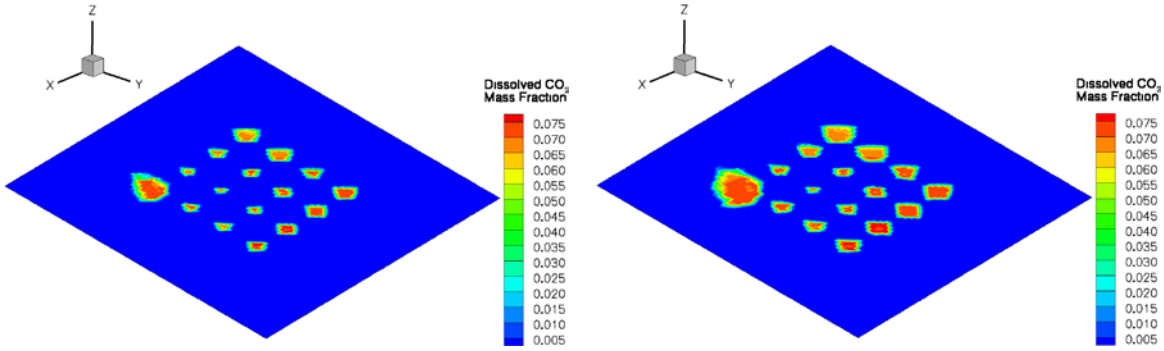


(c) Injecting $CO_2$ for 10 years (d) Injecting $CO_2$ for 20 years

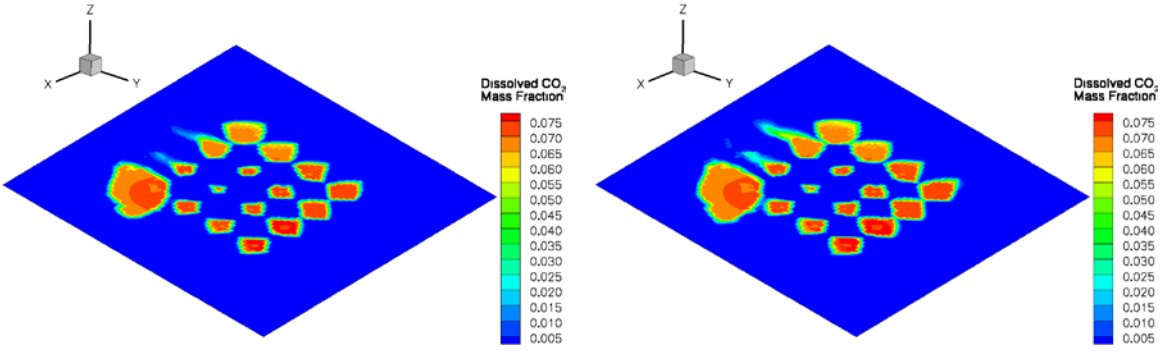


(e) Injecting $CO_2$ for 40 years (f) Injecting $CO_2$ for 50 years

Fig. 15. Contours of the dissolved $CO_2$ fraction contours show CO2 plume increase and migration in the domain during injection of $CO_2$.

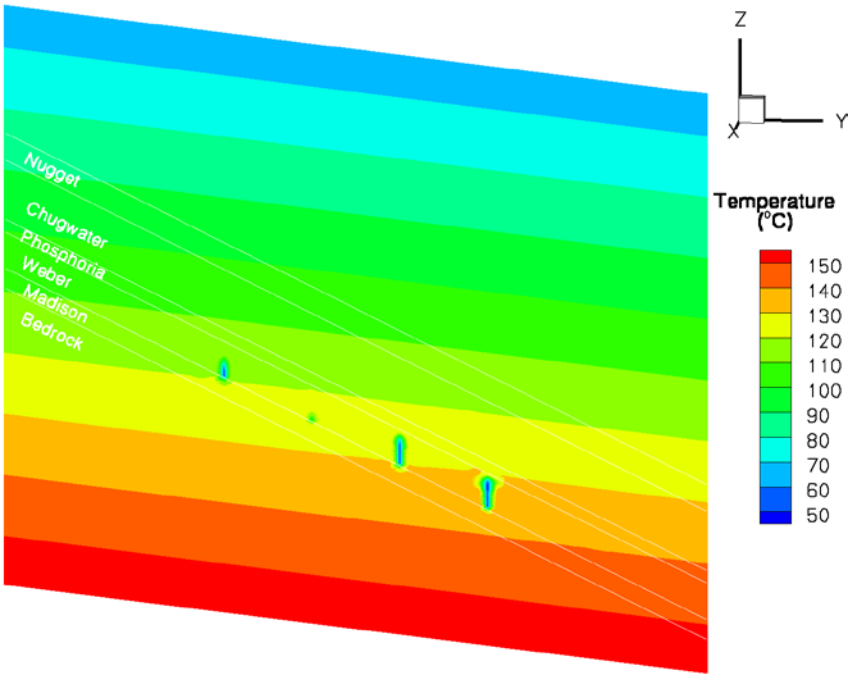


(a) Contours of temperature profile at the end of 50 years of injection of $CO_2$.

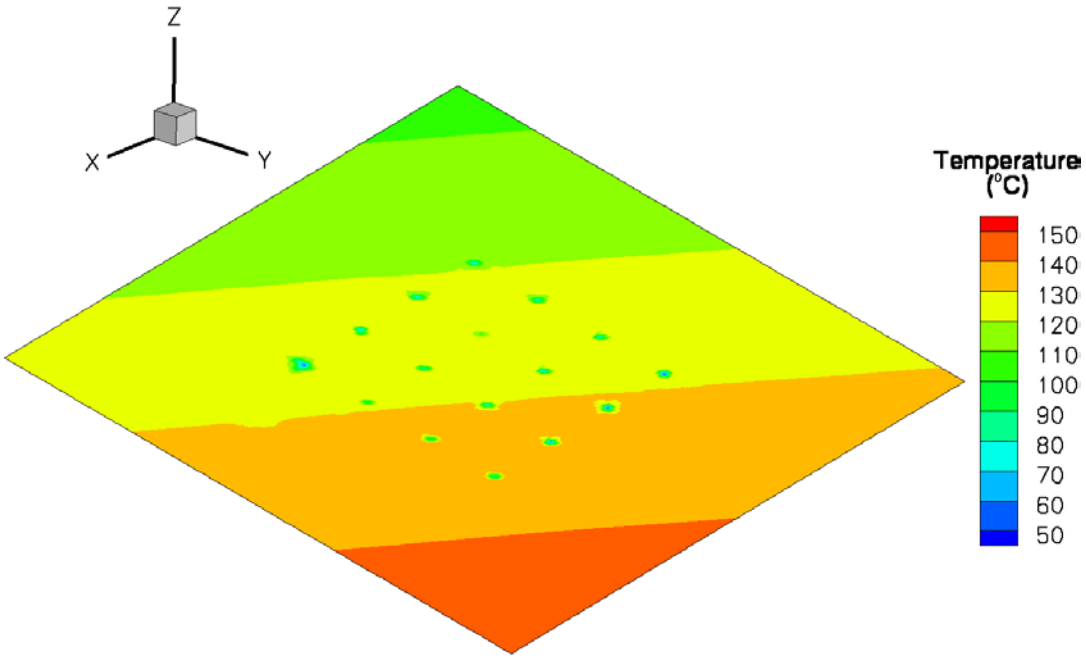


(b) Temperature contour for a horizontal profile at the end of 50 years of injection of $CO_2$.

Fig. 16. Contour of the temperature shows CO2 injection wells have lower temperature than ambient area for 50 years of injection of $CO_2$.

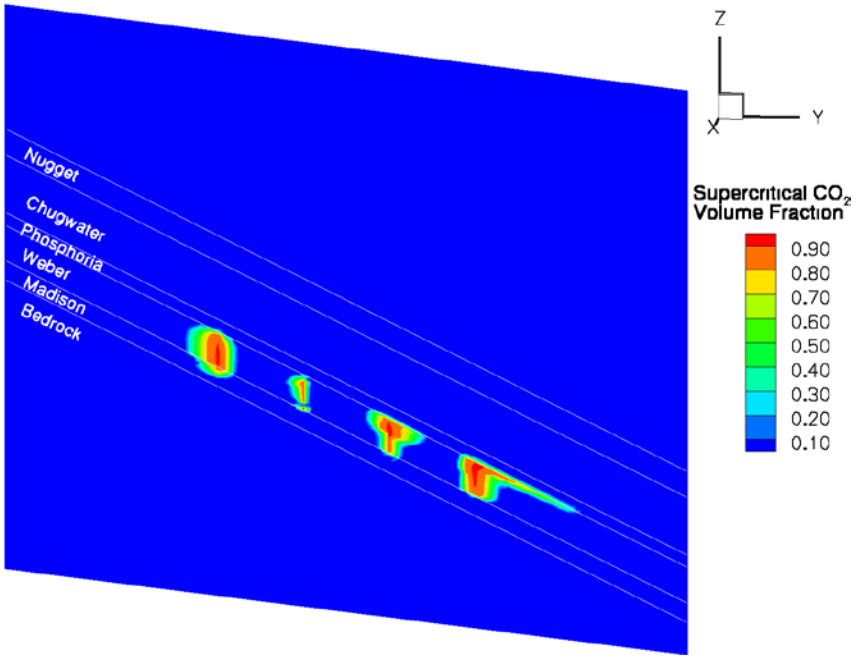


(a) Contour of supercritical $CO_2$ volume fraction shows CO2 leaks into cap-rock at the end of 50 years of injection of $CO_2$.

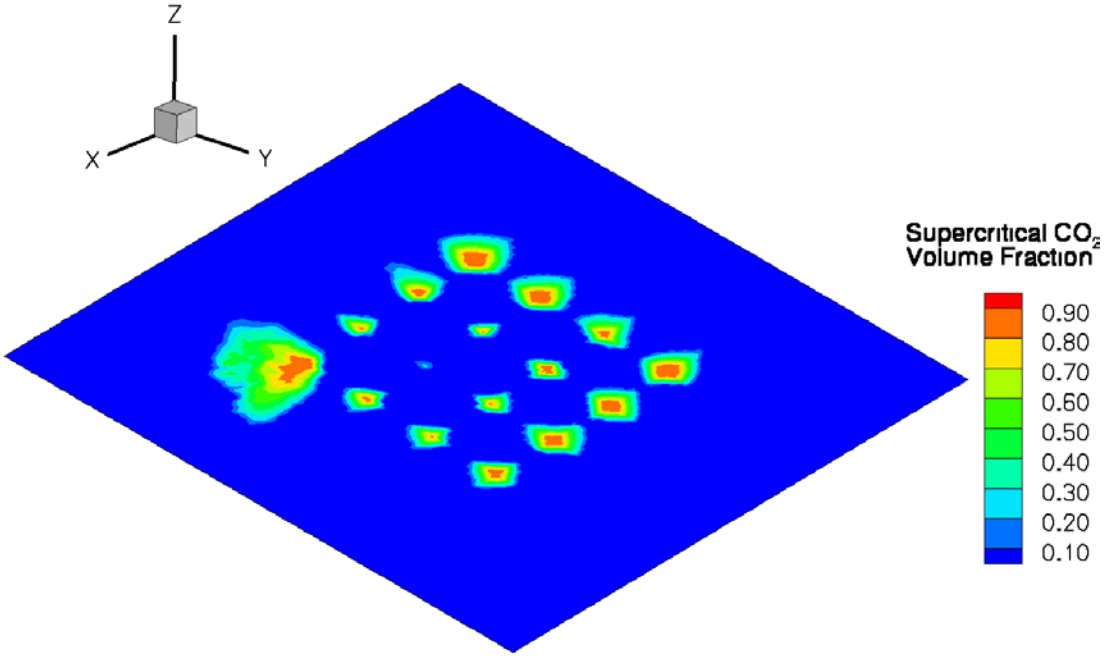


(b) Contour of supercritical $CO_2$ fraction shows CO2 plume grows and migrates in the domain for 50 years of injection of $CO_2$.

Fig. 17. Contour of supercritical $CO_2$ fraction.

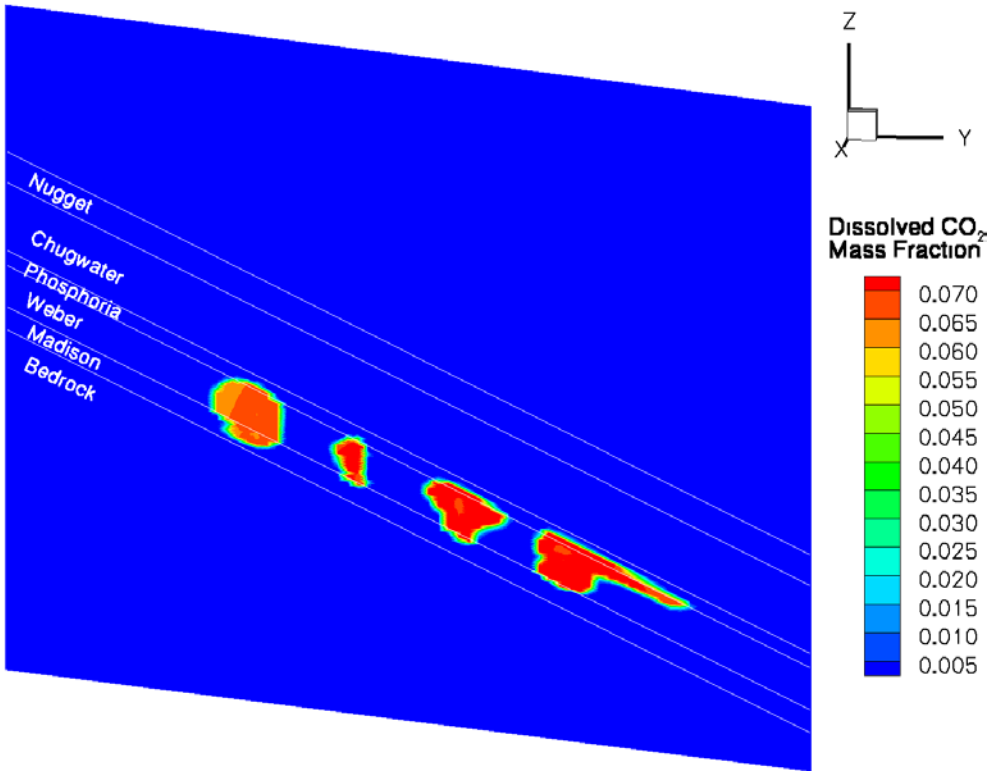


Fig. 18. Contour of dissolved $CO_2$ mass fraction shows CO2 leaks into cap-rock at the end of 50 years of injection of $CO_2$.

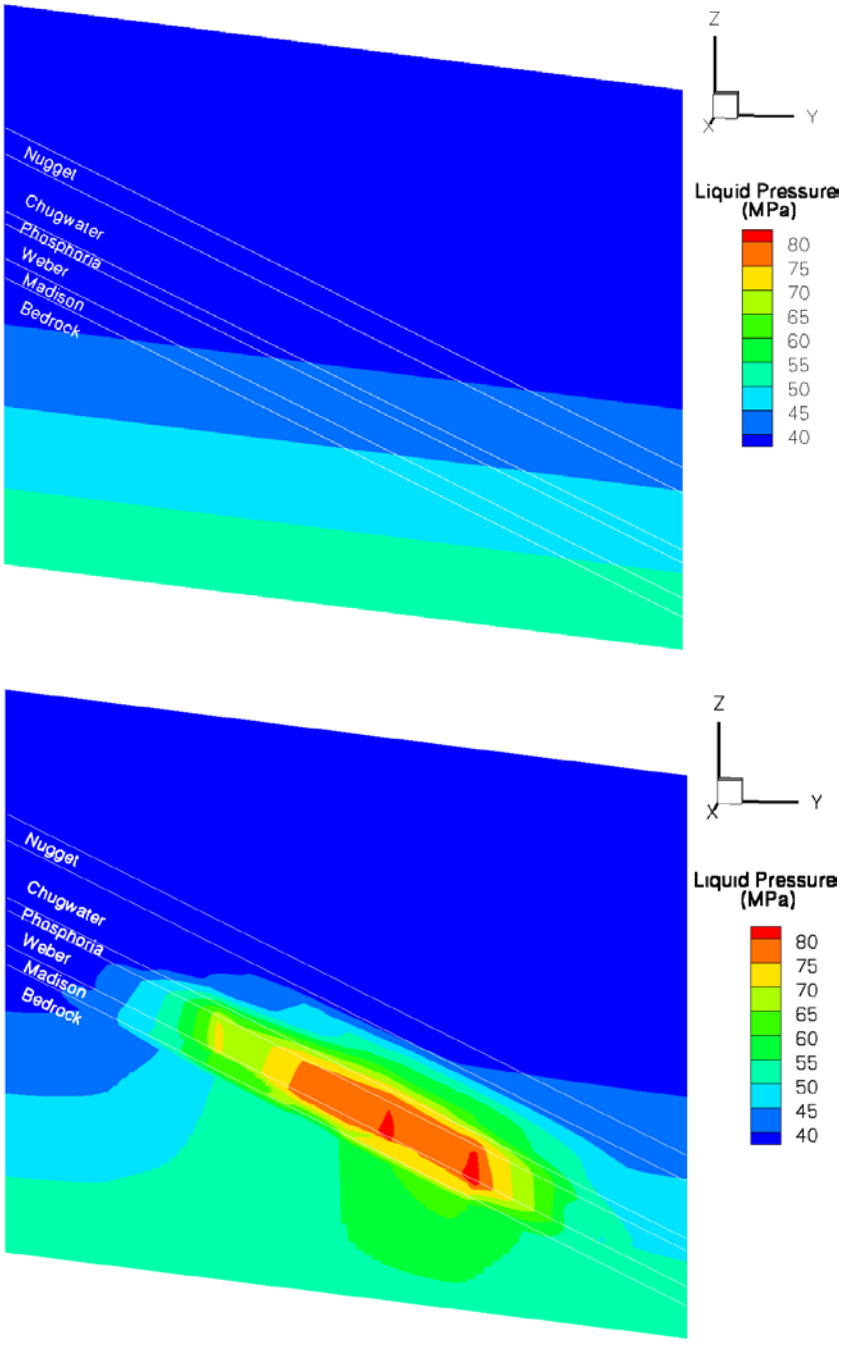


Fig. 19. Contours of the liquid pressure profiles at the beginning and the end of 50 years of injection of $CO_2$.

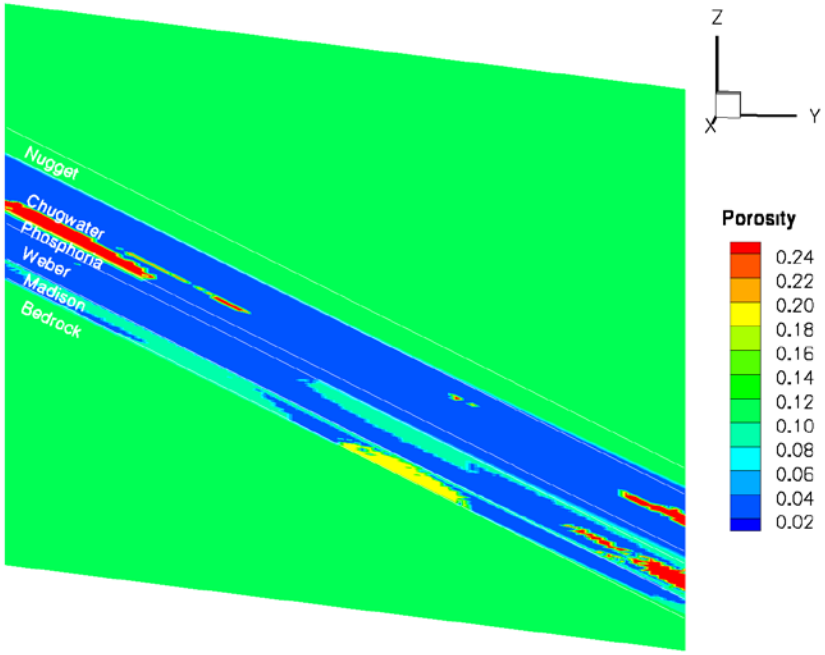


(a)

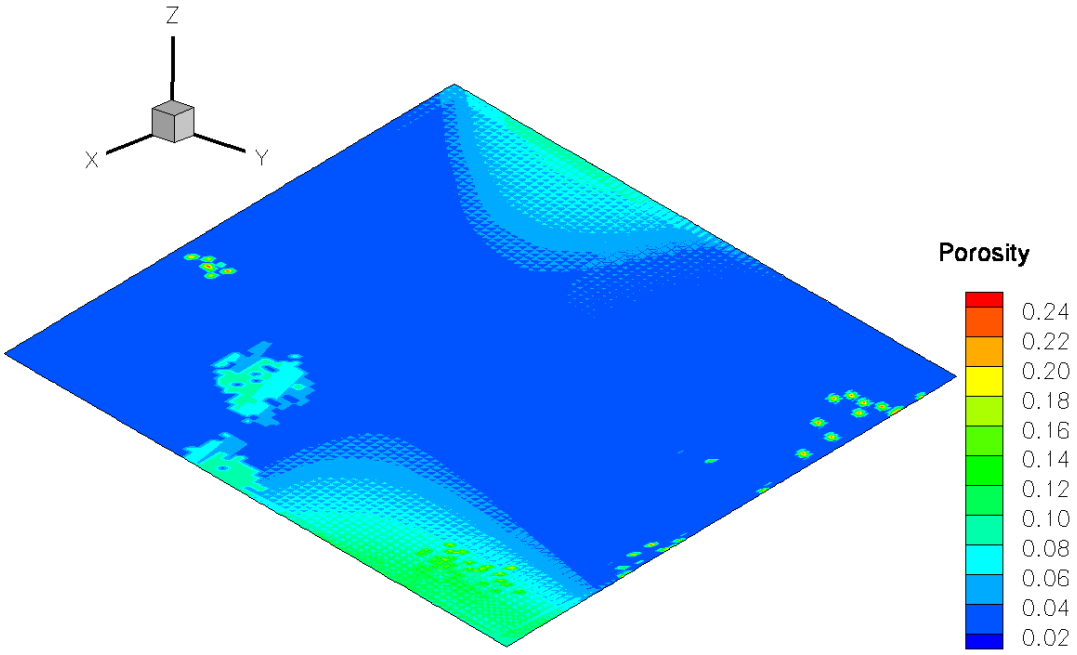


(b)

Fig. 20. Porosity contour.

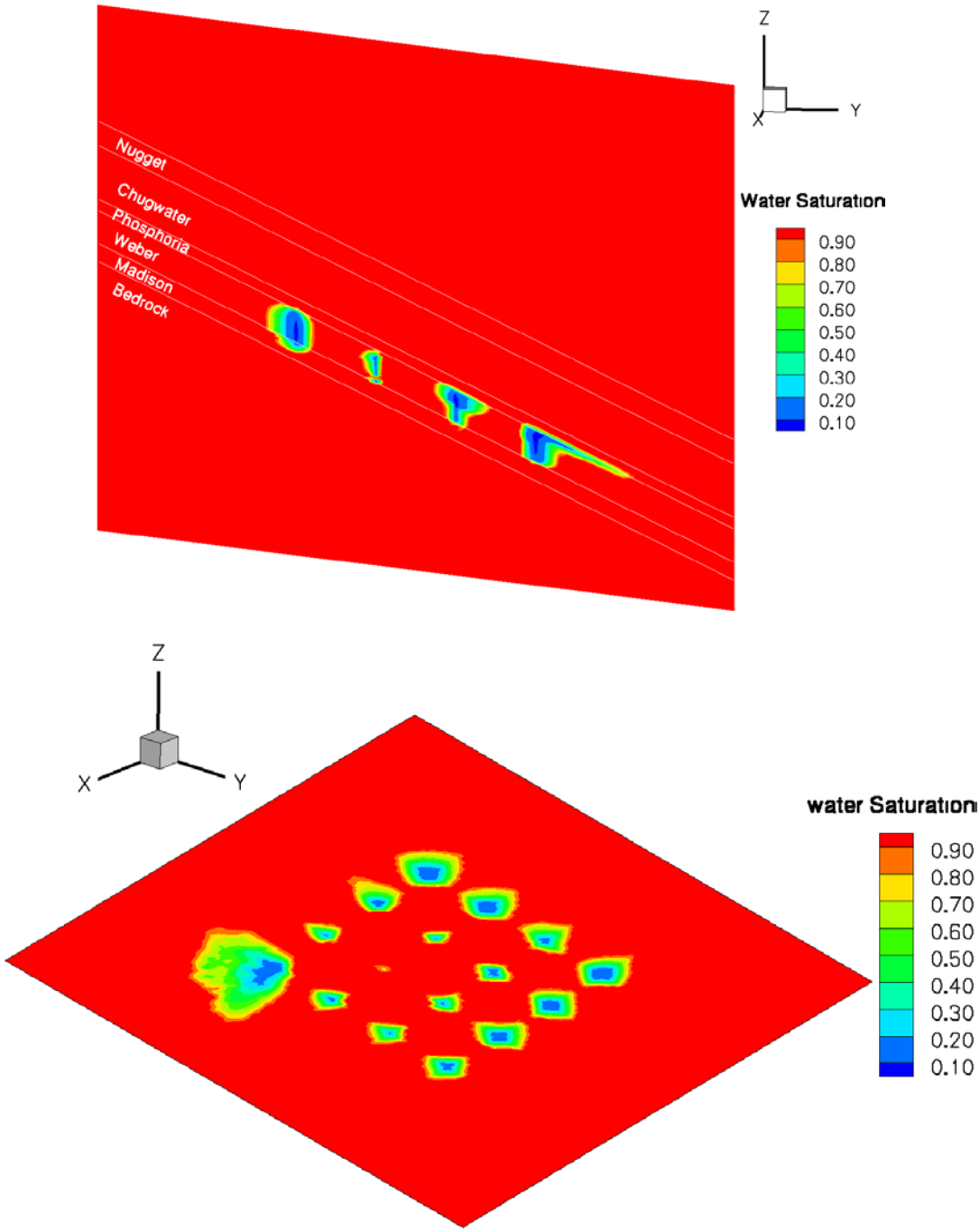


Fig. 21. Contours of the water saturation show CO2 plumes grow and migrate in the domain at the end of 50 years of injection of $CO_2$.

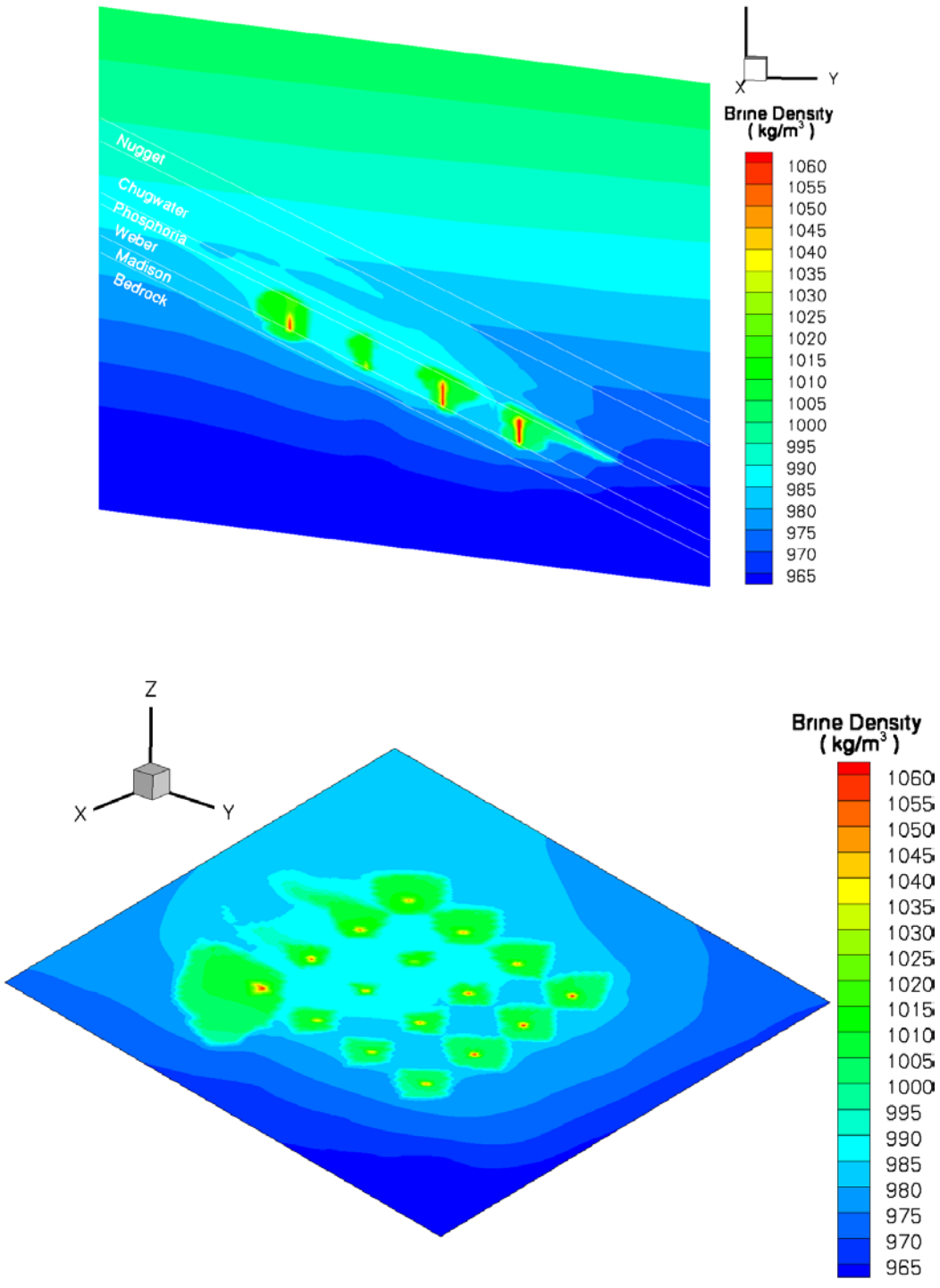


Fig. 22. Contours of the brine Density profile at the end of 50 years of injection of $CO_2$.

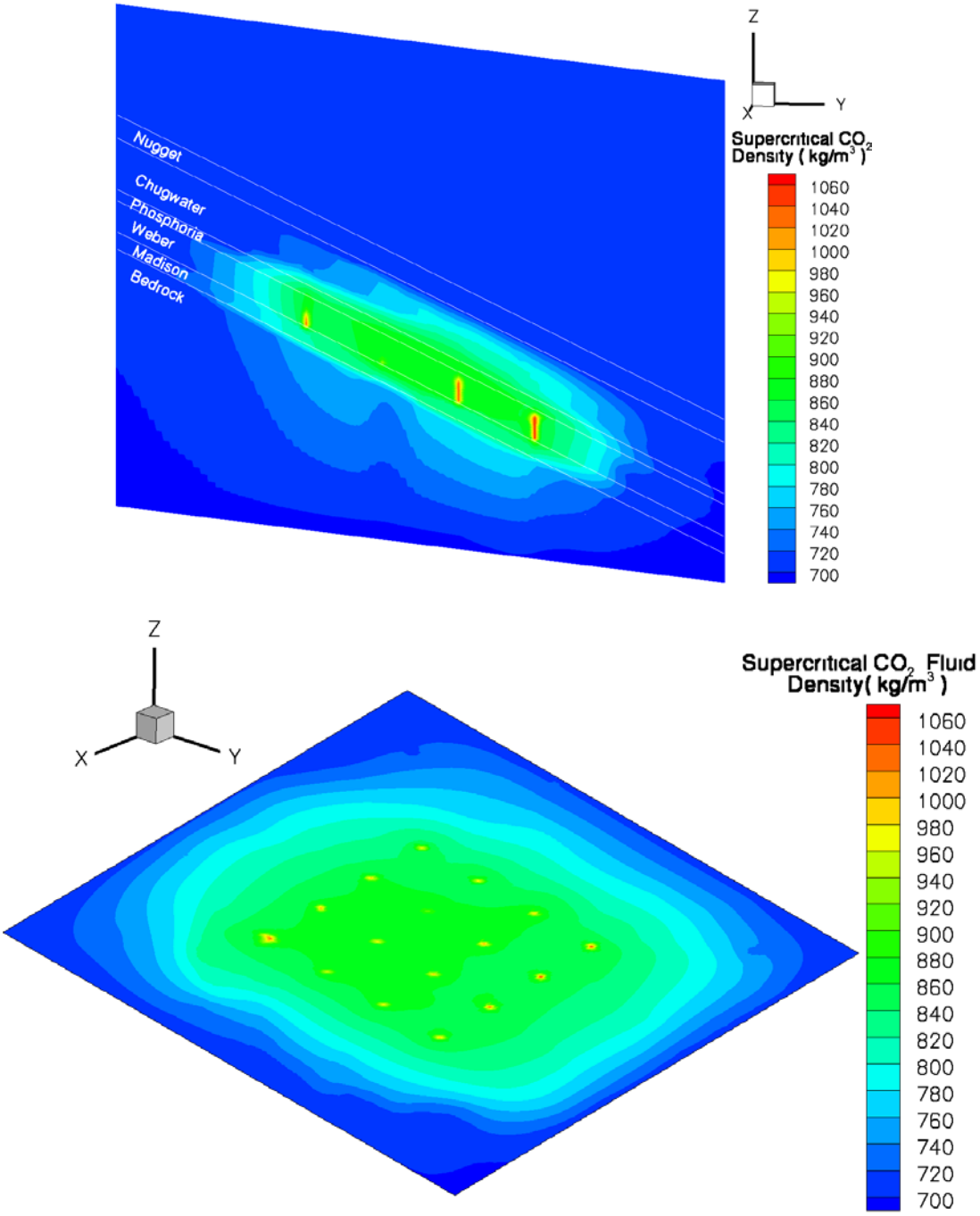


Fig. 23. Contours of the supercritical CO2 fluid density profile at the end of 50 years of injection of $CO_2$.

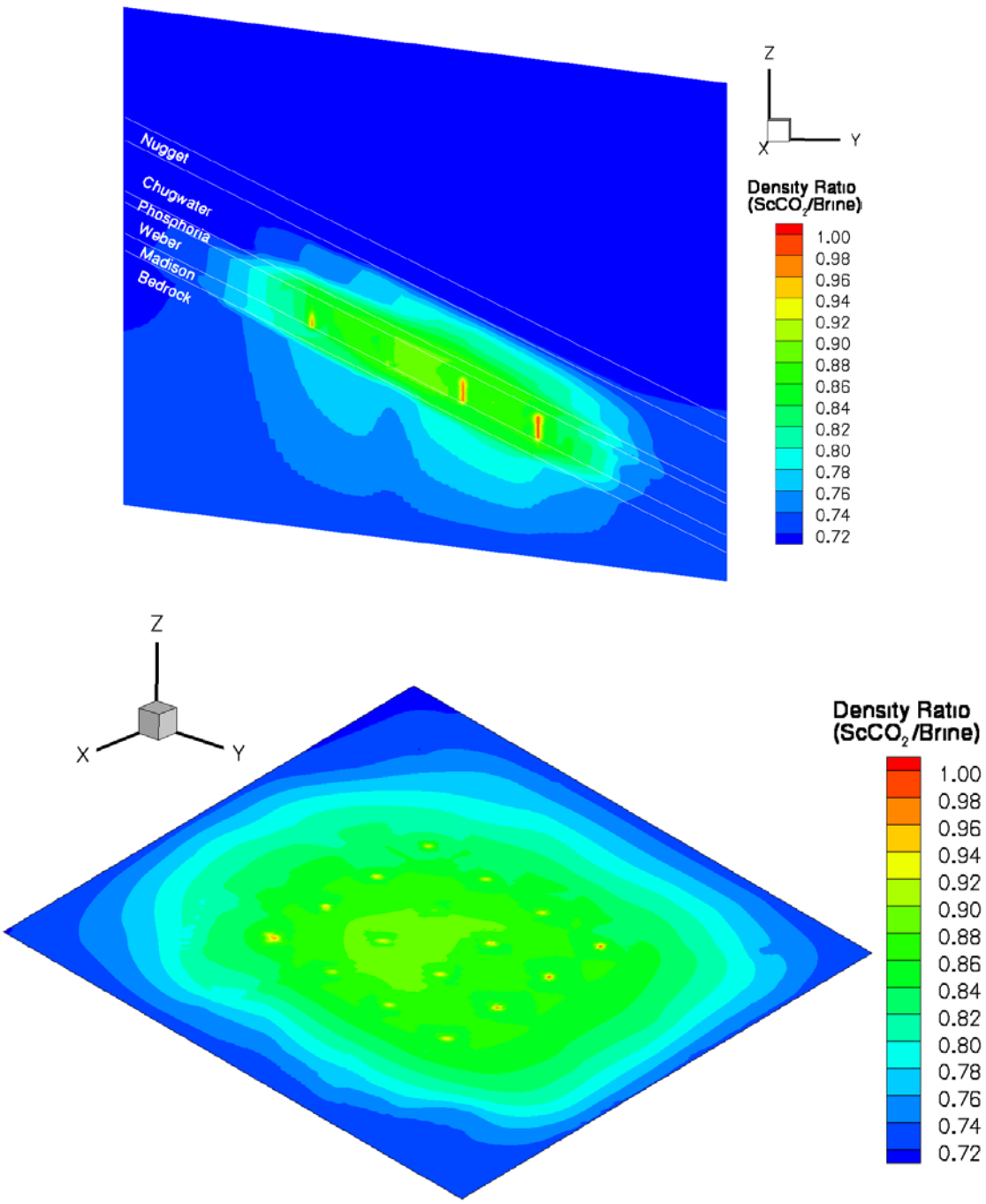


Fig. 24. Contours of the density ratio profile of the supercritical $CO_2$ fluid to brine at the end of 50 years of injection of $CO_2$.

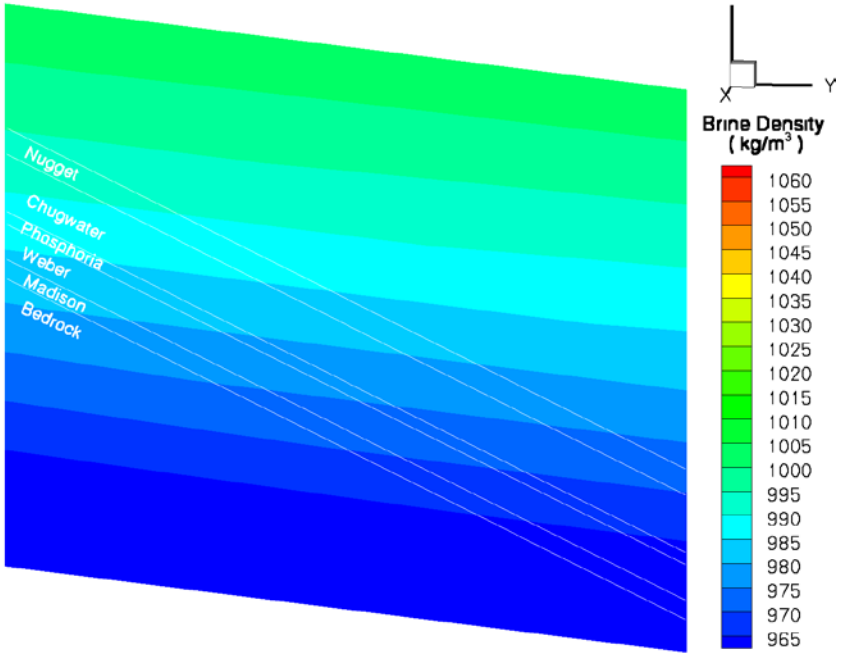


Fig. 25. Steady-state density profiles of the brine before injection of $CO_2$.

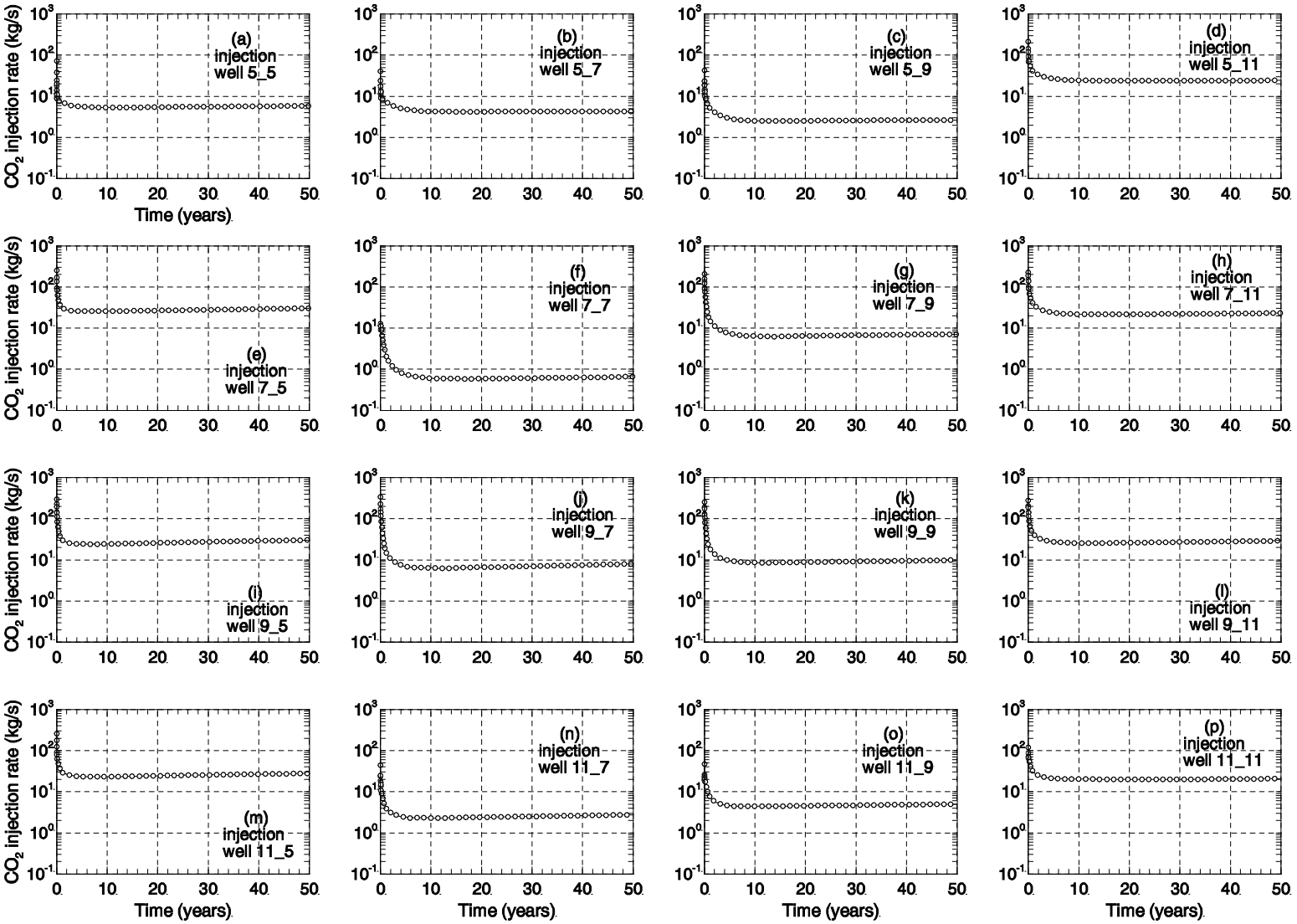


Fig.26. Injection rates change with time in 16 injection wells under condition of constant injection pressure during 50 years of $CO_2$ injection. These variations reflect the huge effects of heterogeneity in saline water aquifer on $CO_2$ sequestration.

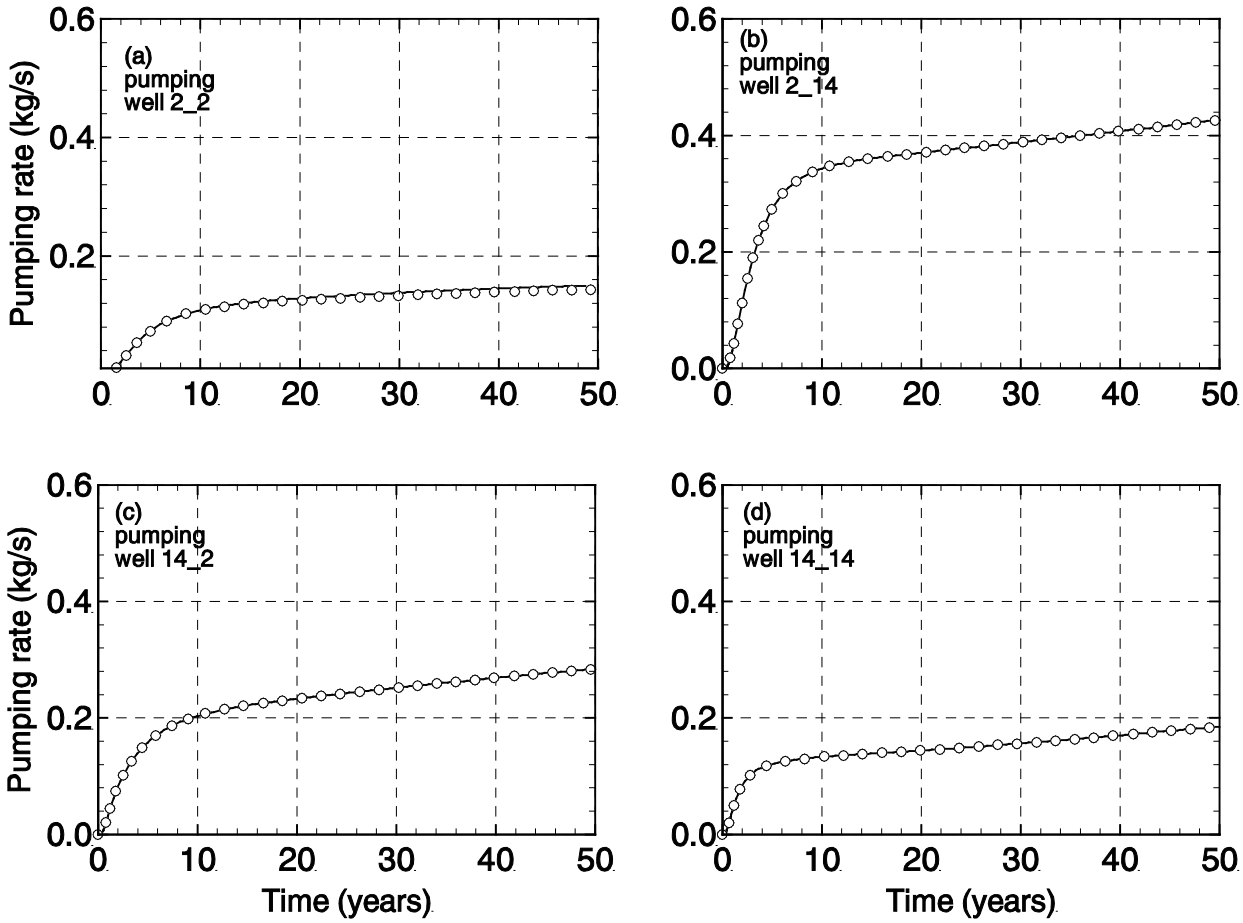


Fig.27. Water pumping rates change with time for 4 pumping wells in the simulation run of perm_6666 under condition of constant pumping pressure during 50 years of $CO_2$ injection.

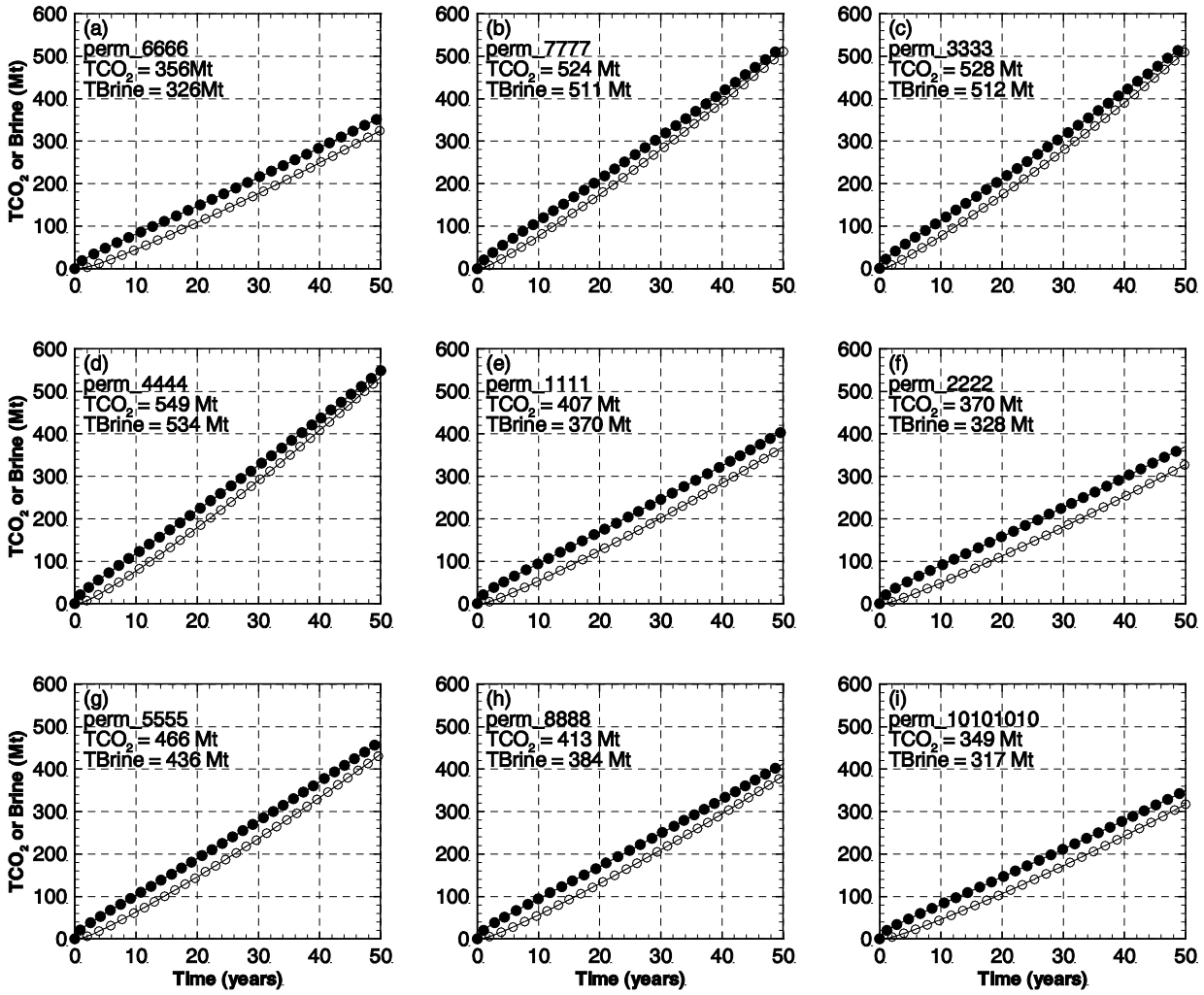


Fig.28. Total injected CO2 and total produced brine for six simulation results with different combination of random permeability field realizations for Chugwater, Phosphoria, Weber and Madison. The square indicates total produced brine and the circle the total injected CO2.

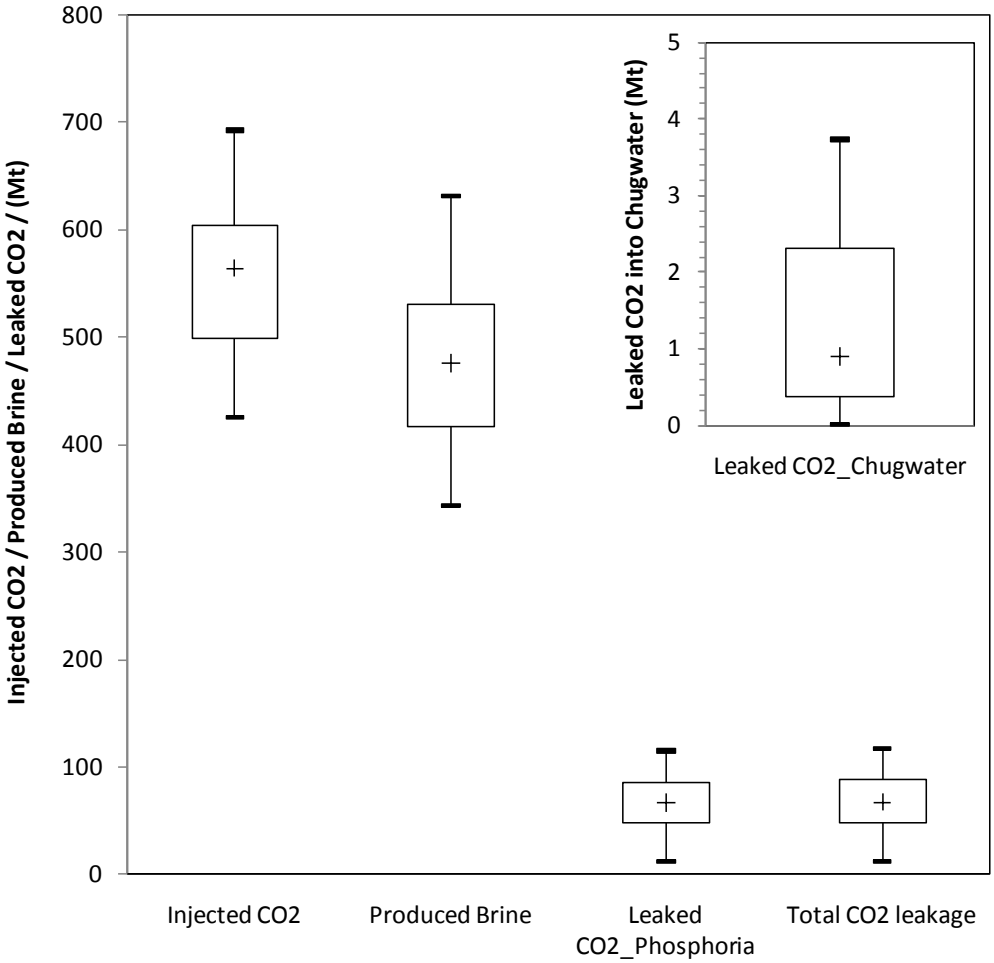


Fig.29. Box plot for injected $CO_2$, produced brine, $CO_2$ leaked into the Phosphoria and Chugwater formations, and total $CO_2$ leakage.

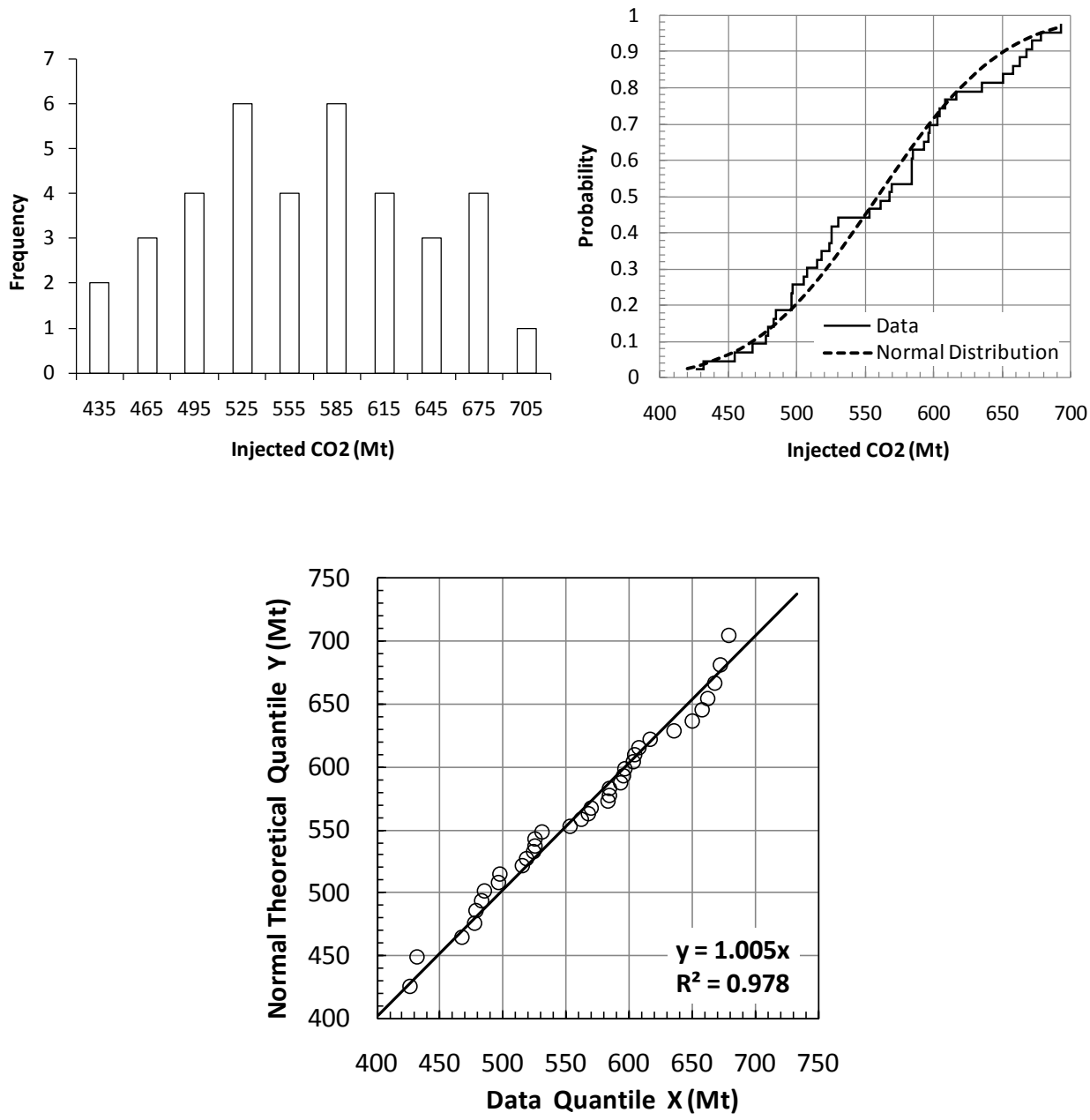


Fig.30. Q-Q plot showing the amount of injected $CO_2$ follows normal distribution.

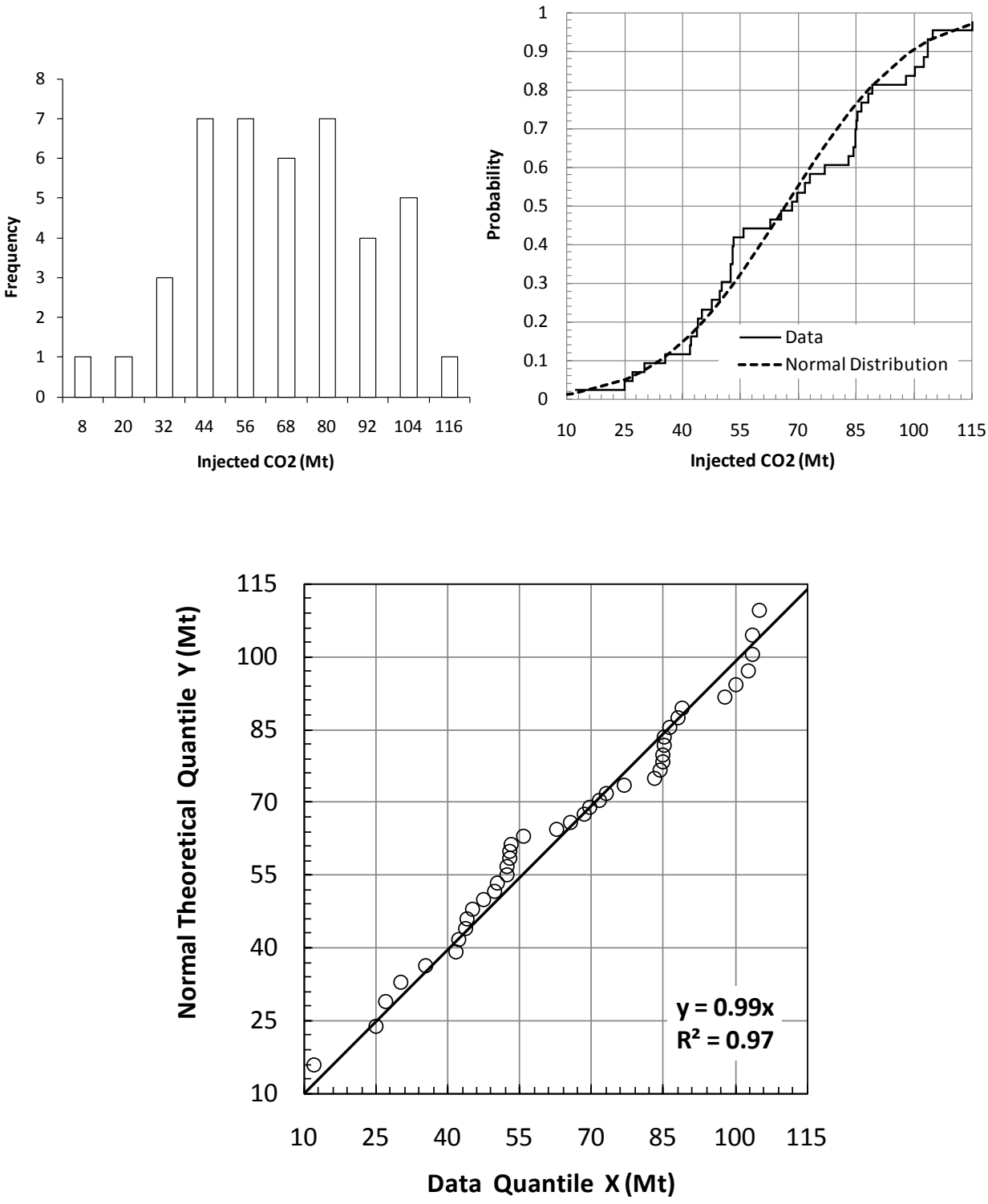


Fig.31. Q-Q plot for $CO_2$ leakage into the Phosphoria formation

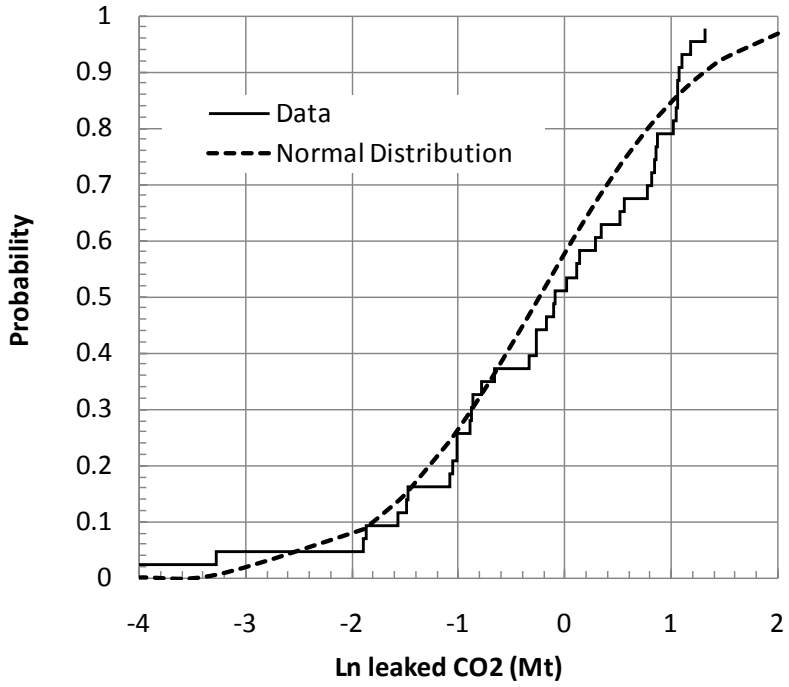


Cumulated distribution function

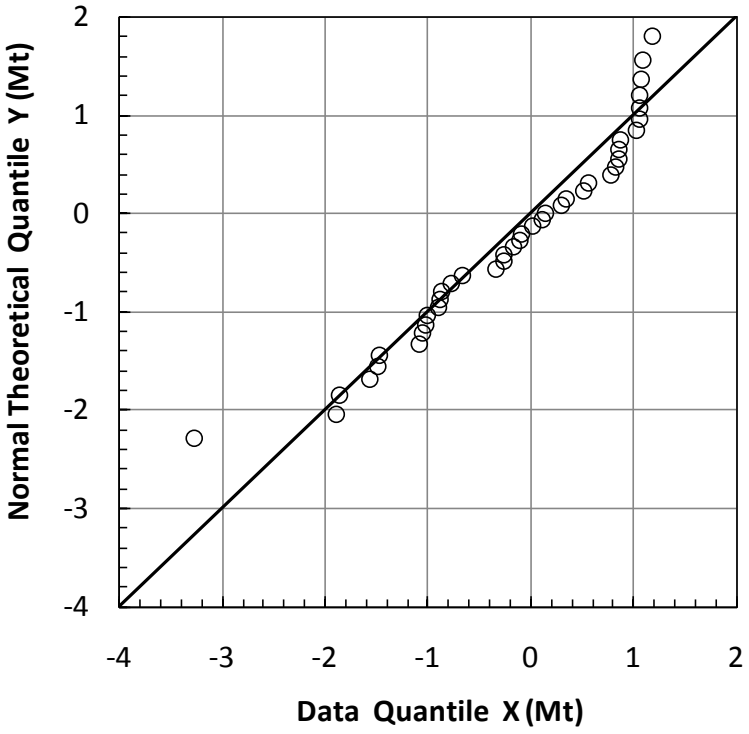


Fig. 32. Q-Q plot showing $CO_2$ leakage into the Chugwater formation. Quantiles of data and the theoretical normal distribution are calculated from natural logarithm transformed values.

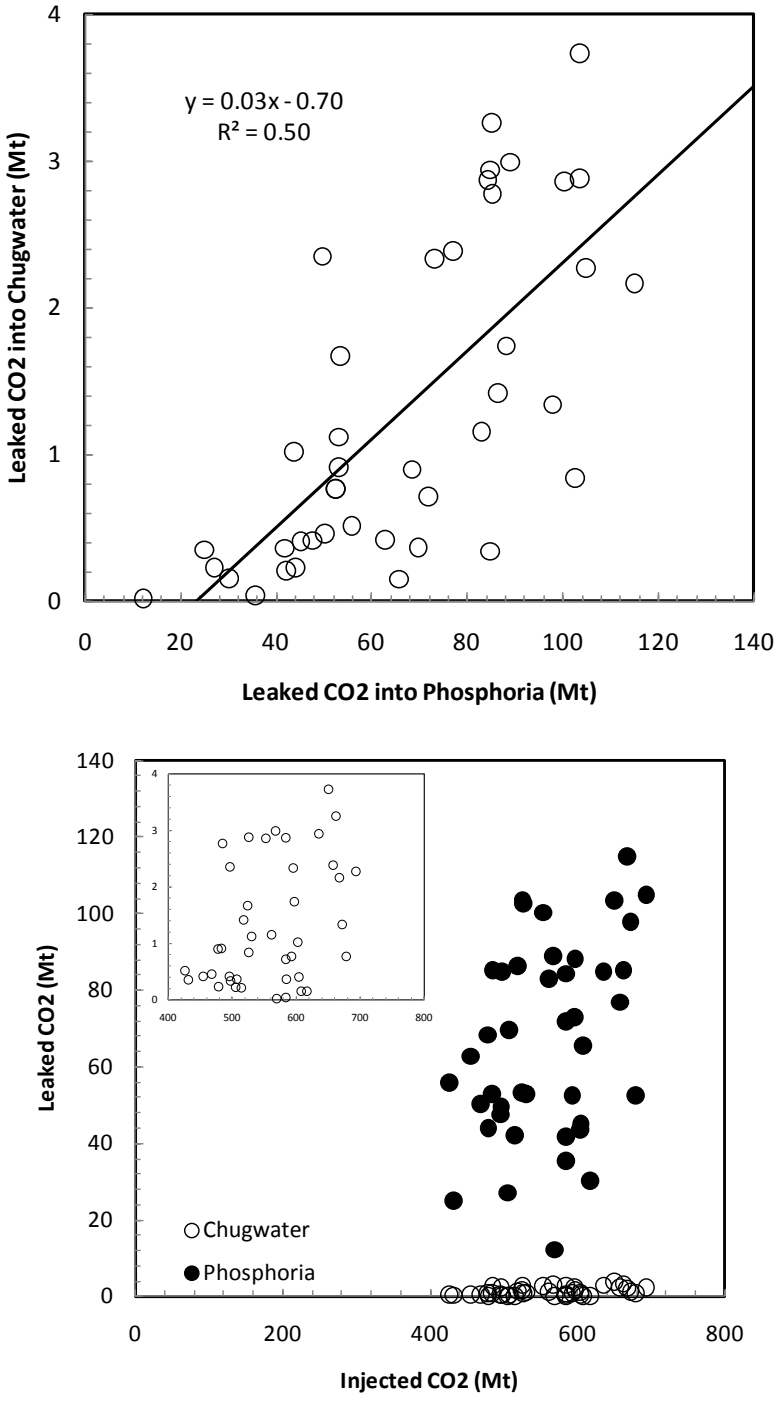


Fig.33. Weak correlation between the leaked $CO_2$ into the Phosphoria and the Chugwater Formations

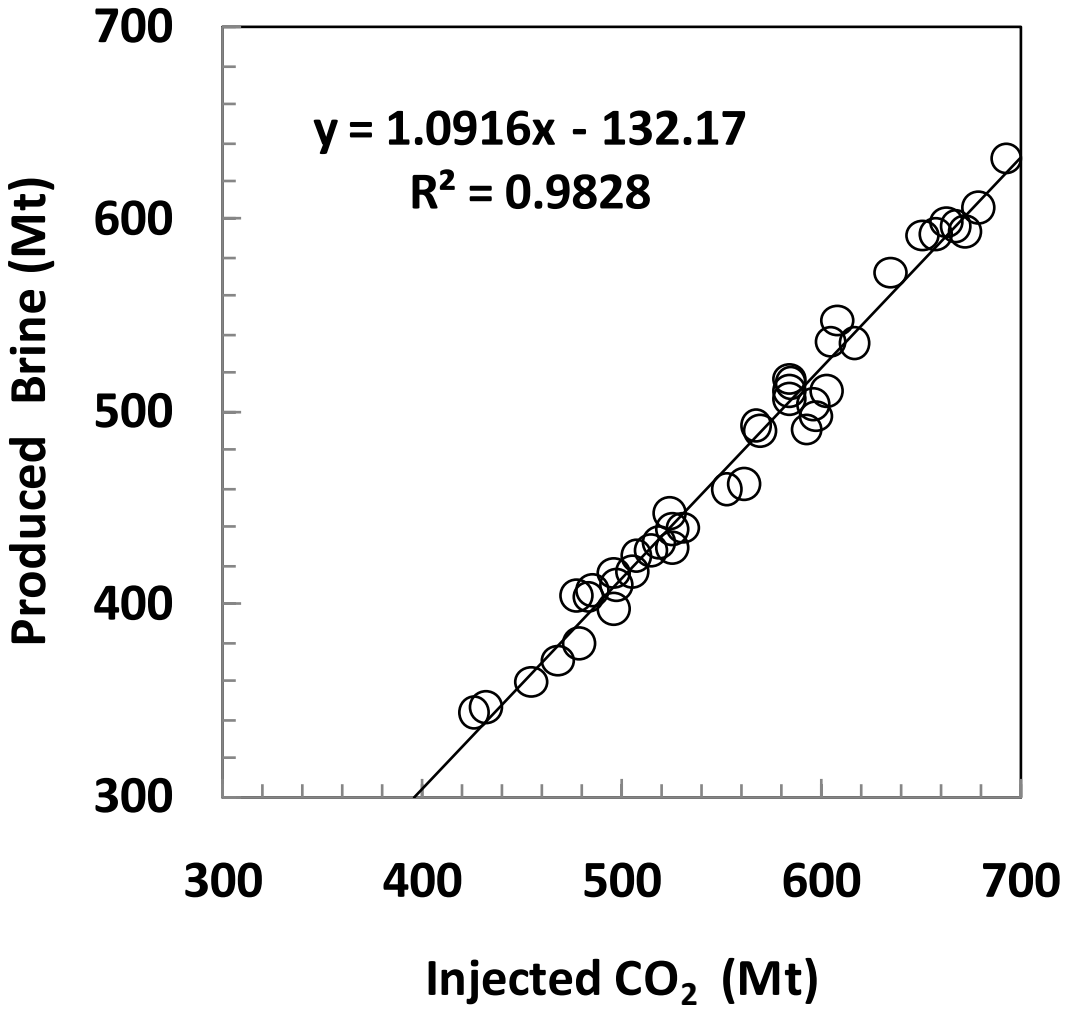


Fig.34. Correlation between injected CO2 and produced brine.